

1 A one-year ACSM source analysis of organic aerosol particle 2 contributions from anthropogenic sources after long-range transport 3 at the TROPOS research station Melpitz

4
5 Samira Atabakhsh¹, Laurent Poulain¹, Gang Chen^{2,3}, Francesco Canonaco^{2,4}, André S. H. Prévôt², Mira
6 Pöhlker¹, Alfred Wiedensohler¹, Hartmut Herrmann¹

7 ¹Leibniz Institute for Tropospheric Research, Leipzig, 04318, Germany

8 ²Laboratory of Atmospheric Chemistry, Paul Scherrer Institute, Villigen, Aargau, 5232, Switzerland

9 ³MRC Centre for Environment and Health, Environmental Research Group, Imperial College London, London, W12 0BZ,
10 U.K.

11 ⁴Datalystica Ltd., Park innovAARE, Villigen, Aargau, 5234, Switzerland

12

13 *Correspondence to:* Hartmut Herrmann (herrmann@tropos.de)

14 **Abstract**

15 Atmospheric aerosol particles are a complex combination of primary emitted sources (biogenic and anthropogenic) and
16 secondary aerosol resulting from aging processes such as condensation, coagulation, and cloud processing. To better
17 understand their sources, investigations have been focused on urban areas in the past, while rural-background stations are
18 normally less impacted by surrounding anthropogenic sources. Therefore, they are predisposed for studying the impact of long-
19 range transport of anthropogenic aerosols. Here, the chemical composition and organic aerosol sources of submicron aerosol
20 particles measured by an aerosol chemical speciation monitor (ACSM) and a multi-angle absorption photometer (MAAP) were
21 investigated at Melpitz from September 2016 to August 2017. The location of the station at the frontier between Western and
22 Eastern Europe makes it the ideal place to investigate the impact of long-range transport over Europe. Indeed, the station is
23 under the influence of less polluted air masses from westerly directions and more polluted continental air masses from Eastern
24 Europe. The OA dominated the submicron particle mass concentration and showed strong seasonal variability ranging from
25 39 % (in winter) to 58 % (in summer). It was followed by sulphate (15 % and 20 %) and nitrate (24 % and 11 %). The OA
26 source identification was performed using the rolling positive matrix factorisation (PMF) approach to account for the potential
27 temporal changes in the source profile (SoFi Pro). It was possible to split OA into five factors with a distinct temporal
28 variability and mass spectral signature. Three were associated with anthropogenic primary OA (POA) sources: hydrocarbon-
29 like OA (HOA, 5.2 % of OA mass in winter and 6.8 % in summer), biomass burning OA (BBOA, 10.6 %, and 6.1 %) and coal
30 combustion OA (CCOA, 23 %, and 8.7 %). Another two are secondary/processed oxygenated OA (OOA) sources: less-
31 oxidized OOA (LO-OOA, 28.4 %, and 36.7 %) and more-oxidized OOA (MO-OOA, 32.8 %, and 41.8 %). Since equivalent
32 black carbon (eBC) was clearly associated with the identified POA factors (sum of HOA, BBOA, and CCOA, $R^2 = 0.87$),
33 eBC's contribution to each of the POA factors was achieved using a multi-linear regression model. Consequently, CCOA

34 represented the main anthropogenic sources of carbonaceous aerosol (sum of OA and eBC) not only during winter (56 % of
35 POA in winter) but also in summer (13 % of POA in summer), followed by BBOA (29 % and 69 % of POA in winter and
36 summer, respectively) and HOA (15 % and 18 % of POA in winter and summer, respectively). A seasonal air mass cluster
37 analysis was used to understand the geographical origins of the different aerosol types and showed that during both winter and
38 summer time, PM₁ (PM with an aerodynamic diameter smaller than 1µm) air masses with eastern influence was always
39 associated with the highest mass concentration and the highest coal combustion fraction. Since during winter time, CCOA is
40 a combination of domestic heating and power plants emissions, the summer contribution of CCOA emphasizes the critical
41 importance of coal power plants emissions to rural-background aerosols and its impact on air quality, through long-range
42 transportation.

43 **1 Introduction**

44 Human health effects of air pollution from particulate matter (PM) are well known, and efforts are being made across the world
45 (*WHO, Expert Consultation, 2019*) to minimize both long-term exposures to harmful levels and air pollution peaks. The
46 submicronic particles known as PM₁ (particles with an aerodynamic diameter less than 1 µm), not only have a negative impact
47 on human health (Pop and Dockery, 2016; Daellenbach et al., 2020) but also have a significant effect on visibility (Shi et al.,
48 2014) and climate (Shrivastava et al., 2017). Its ability to penetrate to respiratory system make it more dangerous, therefore
49 more relevant to mitigate adverse health impact. Since the most numerous component of the atmospheric PM is the organic
50 aerosol (OA) (Jimenez et al., 2009; Chen et al., 2022), contributions to OA and explanations of its chemical and physical
51 characteristics remain challenging, whereas the large variety of OA can be attributed to primary emissions by various sources
52 in different seasons, as well as different reactions to atmospheric dynamics and complicated chemical mechanisms depending
53 on meteorological parameters and geographical locations.

54 In order to evaluate and recognize the sources of OA emission, aerosol mass spectrometers (AMS, Jayne et al., 2000) and
55 aerosol chemical speciation monitors (ACSM) (Ng et al., 2011; Fröhlich et al., 2013) are widely deployed worldwide (Chen
56 et al., 2022; Bressi et al., 2021; Fröhlich et al., 2015). AMS is commonly limited to short time periods due to the high
57 maintenance of the AMS measurements and their high operating costs. As a result, only a few studies run AMS continuously
58 (e.g., see Kumar et al., 2022 and O'Dowd et al., 2014). However, there was still a strong need for such a long-term analysis.
59 ACSM is designated for long-term monitoring purposes due to its robustness and much less labour-intense compared to AMS.
60 Therefore, the deployment of ACSM allows us to look at the long-term (more than one year) temporal changes and/or seasonal
61 variability of OA sources.

62 Regarding the identification of OA sources, source apportionment analysis using positive matrix factorisation algorithm (PMF,
63 Paatero and Tappert, 1994) has been intensively used over the past two decades on both AMS and ACSM measurements (e.g.
64 see Crippa et al., 2014; Poulain et al., 2020). However, this algorithm faced two main limitations when used during a long time
65 period: firstly, the factor profiles are static over the analyzing period (Paatero, 1997); and secondly, rotational ambiguity which

66 provides non-unique solutions. To solve these issues, a multilinear engine (ME-2, Paatero, 1999) has been implemented in the
67 PMF analysis, which allows to use of a priori knowledge to constrain the model to environmentally reasonable solutions (e.g.,
68 Canonaco et al., 2013 and Crippa et al., 2014). To consider the temporal variation of the factor profiles, a rolling approach was
69 suggested (Parworth et al., 2015; Canonaco et al., 2020). The rolling strategy involves advancing a smaller PMF window (i.e.,
70 14 days) and moving/rolling it over the whole dataset to catch the temporal changes of the source profiles with a 1-day step.
71 Although several studies in Europe have already conducted source apportionment analyses of one year or more, most of them
72 were associated with urban or suburban environments (e.g., for urban studies: Stavroulas et al., 2019; Vlachou et al., 2019;
73 Huang et al., 2019; Qi et al., 2020; and for suburban studies: Katsanos et al., 2019; Zhang et al., 2019), and only a few of them
74 were studied in rural-background sites (Schlag et al., 2016; Crippa et al., 2014; Vlachou et al., 2018; Paglione et al., 2020;
75 Dudoitis et al., 2016; Heikkinen et al., 2020; Chen et al., 2021; and Chen et al., 2022), although the rural-background sites
76 represent the major advantage to be able to study the impact of long-range transport of anthropogenic emissions and their
77 changes over a long time period. The Leibniz Institute for Tropospheric Research (TROPOS) Central European observatory
78 Melpitz has been continuously measuring aerosol chemical compositions for 30 years. The station is a unique place in Europe,
79 sitting at the border between marine-influenced Western Europe and continental Eastern Europe. A direct consequence is that
80 the aerosol chemical compositions and mass concentrations strongly depend on the air mass origins, showing less polluted air
81 masses coming from the West and more polluted air masses from the East (Birmili et al., 2010; Spindler et al., 2010). However,
82 only a few studies were done on the source identification of the aerosol reaching the station by covering short time periods
83 mostly during winter (van Pinxteren et al., 2016, 2020).

84 The current study comprehensively investigates the PM₁ aerosol particle chemical compositions and the various OA sources
85 for Melpitz as a rural-background station, based on ACSM and multi-angle absorption photometer (MAAP) measurements
86 from September 2016 to August 2017, using the most advanced rolling PMF with ME-2 implemented in the SoFi Pro package
87 (Datalystica Ltd., Villigen, Switzerland) (Parworth et al., 2015; Canonaco et al., 2013; Canonaco et al., 2020). Although
88 previous papers already considered this dataset, they were focused on quality assurance (Poulain et al., 2020) to depict the
89 European aerosol chemical composition (Bressi et al., 2021 and Chen et al., 2022) or the relationship between the CCN
90 properties (Wang et al., 2022, Schmale et al., 2017), none of these papers were focused on carbonaceous source identification
91 (OA and eBC) nor discussed the strong dependency of the aerosol chemical composition to the air mass origin. Therefore, a
92 multi-linear regression model was used to estimate the contribution of equivalent black carbon (eBC) to the various primary
93 organic PMF factors such as hydrocarbon-like organic aerosol, biomass burning organic aerosol, and coal combustion organic
94 aerosol. Meanwhile, to better understand the emission area of PM₁ chemical composition and PMF factors, the influence of
95 air mass origin was investigated based on self-developed back-trajectory cluster methods (BCLM).

96 **2 Methodology**

97 **2.1 Sampling site**

98 The atmospheric aerosol measurements were carried out at the TROPOS research station Melpitz (51.54° N, 12.93° E,
99 86 m a.s.l.), located approximately 50 km northeast of Leipzig, Germany. The station itself is mainly encircled by agronomical
100 pastures and forests within a rural area, that is why the station is recognized as a rural-background station (Spindler et al.,
101 2013). Since 1992, the station has been monitoring the influence of atmospheric long-range transport on the background air
102 quality of Central European (e.g. Spindler et al., 2012 2013). The Melpitz station is part of EMEP (European Monitoring and
103 Evaluation Programme; Level 3 station, Aas et al., 2012), ACTRIS (Aerosol, Clouds and Trace gases Research Infrastructure),
104 GAW (Global Atmosphere Watch of the World Meteorological Organization), and GUAN (German Ultrafine Aerosol
105 Network, Birmili et al., 2009, 2015, 2016). For a general description of the chemical and physical aerosol characterization
106 analysis techniques, check e.g. Spindler et al., (2004, 2010, 2012, 2013); and Poulain et al., (2011, 2014, 2020).

107 **2.2 ACSM**

108 The chemical compositions and mass loadings of non-refractory PM₁ (NR-PM₁: organic, sulphate, nitrate, ammonium, and
109 chloride) with a 30-minute time resolution were measured by an Aerodyne quadrupole ACSM. The ACSM sampling technique
110 and operational information were previously detailed by Ng et al., (2011).

111 Briefly, after PM₁ transmits across a 100 µm critical orifice, the aerosols are centralized into a narrow beam in an aerodynamic
112 lens (Liu et al., 2007). Non-refractory particulate material that evaporates at the oven temperature (generally 600°C) is recorded
113 and chemically determined using electron impact quadrupole mass spectrometry at 70 eV (Ng et al., 2011). The ions are then
114 detected using a quadrupole residual gas analyser (RGA, Pfeiffer Vacuum Prisma Plus). The ACSM takes 30-second samples
115 of both ambient and particle-free air. The difference in these measurements identifies the aerosol mass spectrum. To change
116 the signal spectra into organic or inorganic species concentrations, the fragmentation table (Allan et al., 2004), the ion
117 transmission correction, and the Response Factor (RF) are applied. To improve the particle loss as a result of bouncing off the
118 vaporizer, the ACSM data were processed according to manufacturer guidelines using a composition dependent collection
119 efficiency (CDCE) correction relying on the algorithms suggested by Middlebrook et al. (2012). Calibrations of Ionization
120 Efficiency (IE) and Relative Ion Efficiency (RIE) were performed using a 350 nm monodispersed ammonium nitrate and
121 ammonium sulphate (Ng et al., 2011). The final mean value for IE was $4.93(\pm 1.45) \times 10^{-11}$ and the mean values for RIEs for
122 ammonium and sulphate respectively were 6.48 ± 1.26 , and 0.68 ± 0.13 . The quality assurance of the ACSM measurements
123 was performed by comparing them with collocated measurements including MPSS, and high-volume filter samples (PM₁ and
124 PM_{2.5}) for the total particle mass concentration, water-soluble ions (nitrate, sulphate, and ammonium), as well as OC/EC.
125 Details on the QA/QC and instrumental uncertainties can be found in Poulain et al., (2020).

126 The ACSM ammonium mass concentration mainly corresponds to ammonium nitrate and ammonium sulphate salts. Previously
127 by Poulain et al. (2020), the neutralization state of the particles was estimated for datasets assuming complete neutralization

128 by nitrate, sulphate, and chloride. Therefore, the particles are neutralized when considering nitrate, ammonium, and sulphate
129 in this study. Furthermore, the significant role of organo-nitrate and organo-sulphate on signals of nitrate and sulphate is not
130 negligible (Kiendler- Scharr et al. (2016). Since the Q-ACSM is working at a unit mass resolution (UMR), it is not possible to
131 distinguish nitrate and sulphate from organic. Therefore, estimating the organo-nitrate would only introduce uncertainties to
132 measurements, therefore, we did not consider to conduct this analysis in this study.

133 **2.3 Additional measurements**

134 In parallel to the ACSM, a MAAP was used to measure the mass concentrations of equivalent black carbon (eBC) (model
135 5012 Thermo Scientific; Petzold and Schönlinner, 2004). The eBC mass concentration from the PM₁₀ data was multiplied by
136 a constant factor of 0.9 following Poulain et al (2011) to estimate the eBC mass concentration in the PM₁ fraction.
137 Consequently, all the eBC mass concentrations reported and discussed here correspond to the eBC in the PM₁ fraction and are
138 referred to as eBC-PM₁. Furthermore, a dual mobility particle size spectrometer (TROPOS-type T-MPSS; Birmili et al., 1999)
139 was used to measure the particle number size distribution (PNSD) from 3 to 800 nm (mobility diameter, d_{mob}) at ambient
140 and 300°C temperatures (Wehner et al., 2002). The MAAP was situated in the same laboratory container as the ACSM and
141 these instruments sampled the same PM₁₀ inlet after a dryer, and the sampled air distribution among the instruments was
142 equally assured by an isokinetic splitter (Poulain et al., 2020).

143 In addition to the online measurements, high-volume samplers (DIGITEL DHA-80, Digitel Elektronik AG, Hegnau,
144 Switzerland) were utilized to capture daily PM_{2.5} samples on a quartz filter (for 24 hours from midnight to midnight). For more
145 details on the sample preparation and evaluation methods, see Spindler et al., (2013). Levoglucosan as a tracer for wood
146 burning combustion was measured following Iinuma et al., (2009) using high performance anion exchange chromatography
147 coupled with an electrochemical detector (HPAEC-PAD).

148 Trace gas measurements were also carried out. Ozone was determined by a U.V. Photometric gas analyser mode 49C (Thermo
149 Scientific, UK), SO₂ by an APSA-360A (Horiba, Kyoto, Japan), and NO and NO₂ using a customized Trace Level NOx
150 Analysis Model 42i-TL (Thermo Scientific) equipped with a blue light converter. Standard meteorological parameters
151 (temperature, relative humidity, solar radiation, precipitation, wind direction, and wind speed) were regularly measured.

152 **2.4 Rolling PMF (ME-2) source apportionment of OA**

153 This work conducted the most advanced source apportionment analysis following a standardized protocol developed by Chen
154 et al., (2022). The PMF method was used to allocate the source of the OA (Paatero and Tappert, 1994) through the Source
155 Finder professional (SoFi Pro, version 8.0.3.1, Canonaco et al., 2021) software package (Datalystica Ltd., Villigen,
156 Switzerland), within the Igor Pro software environment (Igor Pro, version 8.04, Wavemetrics, Inc., Lake Oswego, OR, USA).
157 Two matrices of factor profiles F and factor contributions G , defined the dataset X , and the matrix E named the residual matrix
158 is the fraction which cannot be described by the model. Time series and the chemical fingerprint of sources have been

159 represented by F_{kj} and G_{ik} , respectively. The dimension of F_{kj} and G_{ik} are based on the order p , which is the number of factors
160 selected to represent the data defined by the user:

161

$$162 \quad X_{ij} = \sum_{k=1}^p G_{ik} \times F_{kj} + E_{ij} \quad (1)$$

163

164 In this study, since the measurement covers a period of 12 months (full four seasons), four separate PMF inputs were prepared.
165 Unconstrained PMF was applied with 4 to 6 factor runs for all the seasons; throughout the pre-result and while referring to
166 previous studies (Crippa et al., 2014 and van Pinxteren et al., 2016) primary factors were separated as hydrocarbon-like OA
167 (HOA), biomass burning OA (BBOA) and coal combustion OA (CCOA). However, unconstrained PMF did not result to
168 separate the primary factor profiles. Introducing constraints based on prior knowledge is an efficient strategy for avoiding the
169 mixing of primary factors (Canonaco et al., 2013; Crippa et al., 2014). For this reason, the multilinear engine (ME-2) algorithm
170 (Paatero, 1999) enables the incorporation of time series and factor profiles constraints in form of the a -value approach. In
171 dealing with a profile constraint, the a -value specifies the variety of a factor that can deviate from the anchor profile during
172 the PMF iteration:

$$173 \quad f_{j,solution} = f_j \pm a \cdot f_j \quad (2)$$

174 The constraints applied through ME-2 for HOA and BBOA sources used the anchor profile of Crippa et al., (2014), and Ng et
175 al., (2010), respectively. The anchor profile used for CCOA was generated from our own winter data during this work (SI,
176 1.1). For each of the four seasons, primary profiles were subject to a sensitivity analysis with a -values ranging from 0-0.4 for
177 HOA and BBOA, 0-0.5 for CCOA, and steps of 0.1 to choose the best a -value combination for these three factors.

178 In the PMF approach, there is the intrinsic property of static factor profiles during the period of PMF analysis. Even though
179 for short-term measurements (like one/two season/s) this might be a sensible estimation, long-term observations as are typical
180 for current ACSM study (one year and more), are expected to be subject to evolving factor profiles based on seasonality. To
181 consider the temporal changes, the rolling PMF window method was developed (Canonaco et al., 2021b; Parworth et al., 2015).
182 This technique is applied to a small window, which is slowly extended throughout the whole dataset. Based on the dataset, the
183 user determines the width of the PMF window, the shift parameter, and the number of PMF repeats per window; for the current
184 work, we set 14-day windows, 1-day shifts, and 100 repeats per window.

185 In addition, this rolling PMF analysis was coupled with the bootstrap re-sampling approach (*Bootstrap Methods: Another Look*
186 *at the Jackknife on JSTOR*, 1979), which can randomly select a part of the original matrix and repeat a part of the rows to
187 generate a new same-sized matrix to test the stability of solutions and to estimate the statistical error. Overall, we have
188 combined rolling PMF with ME-2 and bootstrap to conduct the source apportionment investigation, and more information on
189 this new approach was described in Canonaco et al., (2020). This approach for a yearlong dataset generates an enormous
190 amount of PMF runs (N= 35800) and not all of the solutions are environmentally reasonable. Since it is practically impossible
191 to manually inspect all PMF runs, the criterial-base selection was introduced in SoFi Pro to automatically and objectively

192 select environmentally reasonable PMF solutions (Canonaco et al., 2020). Finally, the resulting factors were interpreted as
193 HOA, BBOA, CCOA, and two oxidized OA (OOA) factors named less-oxygenated OOA (LO-OOA) and more oxygenated
194 OOA (MO-OOA). The steps and setups utilized in the evaluation of this dataset are detailed in the supplement (Sect. 1).

195 **2.5 eBC-PM₁ source apportionment**

196 The eBC-PM₁ correlated with each of the three identified primary organic factors (HOA, BBOA, and CCOA) during the source
197 apportionment analysis (Table. 1, which will be discussed later on in the result Sect.). The total amount of these primary factors
198 (known as POA) was highly correlated with eBC-PM₁ ($R^2= 0.87$; Fig. 8a). As a result, the different sources of eBC-PM₁ were
199 evaluated for each factor utilizing a multilinear regression model, as suggested by Laborde et al., (2013); Zhu et al., (2018)
200 and Poulain et al., (2021), for instance. The following assumes that the eBC-PM₁ mass is associated with the separate
201 contribution from each OA factor (i.e., eBC-PM_{1HOA}, eBC-PM_{1BBOA}, and eBC-PM_{1CCOA}) at any time:

$$203 \quad eBC(t) = eBC_{HOA}(t) + eBC_{BBOA}(t) + eBC_{CCOA}(t) \quad (3)$$

204
205 The eBC-PM₁ emission from each source is expected to be proportionate to the separate source mass concentration generated
206 in each season (m_{HOA} , m_{BBOA} , and m_{CCOA} , respectively). As a result, the multilinear regression model can be described as
207 follows:

$$209 \quad eBC(t) = am_{HOA} + bm_{BBOA} + cm_{CCOA} \quad (4)$$

210
211 where a, b, and c are the linear regression coefficients for m_{HOA} , m_{BBOA} , and m_{CCOA} , respectively, that will be applied to evaluate
212 the contribution of eBC-PM₁ per each POA factor for each season (Table. S4).

213 **2.6 Air mass trajectory analysis**

214 Non-parametric wind regressions (NWR) were used to approximate the OA source concentrations at a given wind direction
215 and speed (Henry et al., 2009) in order to investigate not only the local but also the prevalent wind sector associated with
216 transported emission sources (Marin, et al., 2019). The NOAA HYbrid Single-Particle Lagrangian Integrated Trajectory
217 (HYSPLIT-4) model was used to analyse 96 h backward trajectories at 500 m above the model ground of the sampling place
218 (Draxler and Hess, 1997). The trajectory results were used for two independent but complementary analyses to better depict
219 the emission areas of the aerosol: by identifying the potential areas of aerosol sources and by clustering the trajectories.

220 A cluster analysis of the different trajectories was performed. The synoptic-scale air mass condition, together with geographical
221 locations and paths, is a crucial driver of local pollutant concentrations (e.g. Sun et al., 2020; Ma et al., 2014). Local particle
222 mass concentrations and meteorological conditions can play a significant role and be associated with specific air mass

223 trajectories. In addition, the trajectories of the air mass can influence aerosol compositions. For example, the stability of the
224 atmosphere is also meaningful since it influences both the vertical dilution of pollutants and the overall particle mass
225 concentrations. Therefore, the effects of inter-annual variations in air mass conditions and the stability of atmosphere on
226 observed patterns were inspected using a self-developed back-trajectory cluster method (BCLM), concerning air mass
227 backward trajectories, pseudo-potential temperature profiles, PM_{10} mass concentration profiles over Melpitz, and seasons
228 (Birmili et al., 2010; Ma et al., 2014).

229 In this method, the different clusters can be divided according to the different seasons (CS: cold season; TS: transition season;
230 and WS: warm season), and meteorological synoptic patterns (ST: stagnant; A1: anticyclonic with air mass coming from
231 Eastern Europe; A2: anticyclonic with air mass coming from the west; C1: cyclonic with air mass coming from relatively
232 south; C2: cyclonic with air mass coming from the west and south west). However, the clustering approach did not consider
233 spring and fall separately, and therefore the transition clusters correspond to both spring and fall. Finally, a total of fifteen
234 clusters were identified, corresponding to different meteorological conditions over the course of the year. Descriptive analysis,
235 cluster processing, and data processes and products are all described in detail by Sun et al., (2020) and Ma et al., (2014).

236 **3 Results and discussion**

237 **3.1 PM_1 chemical composition**

238 In this work, we investigate one-year-long measurements of PM_1 for Melpitz, Germany. All the data are presented in UTC,
239 during the winter and summer, the time zone is one and two hours behind local time, respectively. Yearly time series, seasonal
240 variation, and diurnal cycles of aerosol particle chemical compositions including mass concentrations and mass fractions, as
241 measured by ACSM and MAAP, are shown in Figures 1, 2, and 3, respectively. Over the entire period, the chemical
242 composition of PM_1 was basically made up of organic aerosol (46 % of the total mass; Fig. 1c), sulphate (16 %), nitrate (21
243 %), ammonium (11 %), eBC- PM_1 (6 %), and chloride (close to 0 %). However, a mean mass concentration of $10.49 \mu\text{g}/\text{m}^3$
244 (Fig. 1) was obtained with an obvious seasonal trend which detected the highest total mass concentration ($15.95 \mu\text{g}/\text{m}^3$) during
245 the winter time and lowest mass concentration during the summer time; $6.24 \mu\text{g}/\text{m}^3$ (Fig. 1a and Fig. 2a). Compared to previous
246 AMS measurements of Poulain et al., (2011) at the same station, a similar seasonal trend was observed in the period 2008/2009,
247 while the absolute masses differed (Table. S1), which is at least partially related to the inter-annual changes of the
248 meteorological conditions. Compared to previous ACSM long-term measurements of Poulain et al., (2021) at the same station,
249 a similar mean mass concentration of PM_1 was observed in the period from June 2012 to November 2017 (Poulain et al., 2021:
250 $10.23 \mu\text{g}/\text{m}^3$ and this study: $10.49 \mu\text{g}/\text{m}^3$; respectively), and presented same seasonal trends for all the chemical species (Table.
251 S2) with a highest mass concentration in the winter and lowest mass concentration in the summer time ($13.15 \mu\text{g}/\text{m}^3$ and 7.64
252 $\mu\text{g}/\text{m}^3$, respectively; Table. S2). Consequently, the results obtained from the current study can be considered as a representative
253 ACSM study for Melpitz station. Fig. S3 presents the coming high polluted air masses for total PM_1 to the measurement site

254 in the current study; polluted Eastern Europe flow with high mass concentration and south-west with lower mass concentration
255 was more clearly found in winter time rather than in other seasons, which will be comprehensively discussed in the Sect. 3.4.
256 In comparison with other ACSM/AMS rural-background stations in Europe which can be divided into three parts Northern
257 Europe (NE), Southern Europe (SE), and Mid-latitude Europe (ME) (Bressi et al., 2021), the annual PM₁ mean mass
258 concentration measured at Melpitz is similar to the value obtained at other ME stations, such as Magadino 10.1 µg/m³, Kosetice
259 8.5 µg/m³ (Chen et al., 2022), 9.1 µg/m³ on average of PM₁ mean mass concentration of 6 stations (Ispra, Melpitz, Magadino,
260 Cabauw, Sirta, and Hohenpeissenberg, Bressi et al., 2021).

261 **3.1.1 Inorganic**

262 The seasonality of the inorganic species can be associated with their variations in emissions and/or the changes in their
263 chemical atmospheric processes. Throughout the year, the mass concentration and their respective contribution to the total
264 PM₁ mass of nitrate, ammonium, and chloride increased from a minimum value in summer (11 %, 7 %, and 0 %, respectively;
265 Fig. 2b) and reached a maximum value in winter (24 %, 12 %, and 1 %, respectively; Fig. 2b). Moreover, the comparison
266 between Bressi et al., (2021) and current study (Fig. S4 from Bressi et al 2021, Fig. 3 from the current study) for Melpitz
267 station with different time coverage shows that the daily variation of ACSM sulphate, nitrate, and ammonium are similar in
268 both winter and summer seasons. In comparison with other ACSM/AMS rural-background stations in Europe (Fig. S4, Bressi
269 et al., 2021), the mean daily cycle of the PM₁ chemical components (sulphate, nitrate, and ammonium) does not show a similar
270 pattern to the other stations (Bressi et al., 2021) due to the different geographical location and meteorological conditions.

271 Sulphate showed a slightly different behavior. Although the contribution of sulphate to the total PM₁ decreased slightly from
272 summer (20 %) to winter (15 %), its mass concentration remained higher in winter compared to summer (2.38 µg/m³ and 1.23
273 µg/m³, respectively; Table. 1). The increment is not as drastic as other inorganic species since sulphate is least volatile,
274 therefore, more fraction of sulphate stayed in particle phase even in summer. Moreover, the sulphate contribution to the total
275 PM₁ was higher during the summer than winter time, since with enhanced irradiations in summer, sulphate formation from
276 photochemistry could be enhanced as well. This sulphate higher contribution in summer over winter is consistent with the
277 mean PM₁ mass concentration measured by AMS for the three periods during fall (16. September.2008 to 03. November.2008),
278 winter (24. February.2009 to 25. March.2009), and summer (23. May.2009 to 09. June.2009) campaigns reported by Poulain
279 et al., (2011). In comparison with previous ACSM long-term measurements of Poulain et al., (2021) at Melpitz station, a
280 similar mean mass concentration of sulphate was observed in the period from June 2012 to November 2017 (Poulain et al.,
281 2021: 1.54 µg/m³ and this study: 1.67 µg/m³; respectively; Table. S2). This comparison indicates the current study as a case
282 study of ACSM for Melpitz station within 5-year ACSM data, with the best data coverage of time in a year. The diurnal cycles
283 of sulphate (Fig. 3) showed a different daily pattern in warm and cold seasons. In summer, sulphate mass concentration
284 increased during the day and reached its maximum level at 12:00 UTC (Fig. 3) due to sulphur dioxide photochemical oxidation
285 processes in the atmosphere, which also presented the highest mass concentration during the day, along with maximum
286 temperature and sun radiation in summer time (Fig. S4). Furthermore, the NWR plots (Fig. S3) show that during the winter

287 time, sulphate mostly comes from the north and east sectors with wind speeds above 5 m/s which can be associated with
288 dominant transported sulphate sources. Although the eastern wind sector remains visible for the sulphate in the summer time,
289 the high concentrations of sulphate can be observed during periods with low wind speed and without a specific wind sector;
290 which corresponds to local sulphate formation. Sect. 3.4 will go into detail about the long-range transported emissions later
291 on. Although this locally formed emissions of sulphate (Fig. S3 and Fig. 9) can explain this peak during the day in summer,
292 this photochemical process is not the only source of sulphate. It especially cannot explain the highest mass concentrations
293 during the winter time with almost no diurnal variation (Fig. 3). For winter, the emission of domestic heating processes, which
294 could be enhanced in the atmospheric boundary layer (Stieger et al., 2018), along with the long-range transported emissions,
295 which came from north-east toward the measurement site (Fig. S3 and Fig. 9), and also high ammonium nitrate due to
296 partitioning according to temperature, explain the high mass concentration but the low relative contribution of sulphate.

297

298 Nitrate is mostly found in the form of ammonium-nitrate (NH_4NO_3), which is reliant on the gas phase precursor concentrations,
299 temperature, humidity, and aerosol chemical composition (Poulain et al. 2011; Stieger et al., 2018). Both nitrate and
300 ammonium showed a minimum mass fraction and mass concentration in summer (11 %, $0.68 \mu\text{g}/\text{m}^3$, 7 %, $0.43 \mu\text{g}/\text{m}^3$,
301 respectively; Fig. 2), an increasing trend toward the cold months and reached their maximum mass fraction and mass
302 concentration in winter time (nitrate 24 %, $3.87 \mu\text{g}/\text{m}^3$, ammonium 12 %, $2 \mu\text{g}/\text{m}^3$, respectively; Fig. 2). The diurnal cycles of
303 nitrate and ammonium (Fig. 3) showed a relatively similar daily pattern in all seasons, which means the highest values were
304 reached in the morning, due to the beginning of vertical mixing and a reduction in the afternoon followed by an increase during
305 the night, reflecting their night time production during every season. The volatile behaviour of ammonium-nitrate strongly
306 affects its temporal variation during warm days leading to the formation of the gaseous nitric acid and ammonia compounds
307 at higher temperatures and low humidity (Fig. S4, and S8). Nitrate profiles from NWR plots (Fig. S3) present two different
308 wind directions for the whole period which might be associated with transported nitrate from Leipzig and Torgau (50 km in
309 the south-west and 7 km in the north-east of Melpitz, respectively) with higher wind speed. Since the reaction pathway of OH
310 and NO_2 can result in nitrate formation (Yang et al., 2022), this mechanism can be linked to traffic emissions in residential
311 areas. These long-range transported sources together with locally formed emissions could describe higher mass concentrations
312 for nitrate and ammonium due to e.g., meteorological conditions and abundant precursors in winter time. However, in winter,
313 ammonium-nitrate remains mainly in the particle phase (Seinfeld and Pandis, 2006) since it can totally be changed from gas
314 to particle phase at lower temperature (Spindler et al., 2010). High values of nitrate and ammonium in spring time are linked
315 to agronomical fertilization (Stieger et al., 2018). These seasonal contribution results for both, nitrate and ammonium, are
316 consistent with the previous AMS study (Poulain et al., 2011), with minimum fraction to the total AMS- PM_1 during summer
317 (nitrate 5 % and ammonium 8 %; Table. S1), and maximum fraction during winter time (nitrate 34 % and ammonium 17 %;
318 Table. S1). However, it is known that a fraction of the nitrate signal can be attributed to nitrogen containing organic species
319 (Kiendler-Scharr et al., 2016), which can affect the overall nitrate mass concentration (Poulain et al., 2020).

320

321 Although chloride had the lowest annual mass concentration ($0.05 \mu\text{g}/\text{m}^3$) compared to all other PM_1 chemical components
322 (Table. 1), it showed the highest mass concentration and mass fraction in winter ($0.11 \mu\text{g}/\text{m}^3$, 1 %, respectively; Fig. 2a&b;
323 Table. 1) compared to other seasons; as seen in the previous AMS study of Poulain et al., (2011) (2 %, Table. S1). It could be
324 related to the surrounding and transported emissions which mass concentrations were high for air masses from north-easterly
325 and south-westerly directions (Fig. S3). In a multi-year analysis of the hourly PM_{10} chloride mass concentration measurements
326 using a MARGA, Stieger et al., (2018) attributed the chloride sources of Melpitz during winter to the resuspension of road salt
327 used for the de-icing of streets, mainly coming from the cities of Torgau and Leipzig. These sites are also located in the wind
328 directions along with the coal and wood combustion emission region, which could explain the highest mass concentration of
329 chloride during the winter. Furthermore, the existence of chloride might be due to low mass concentration marine influences
330 consisting of sea-salt aerosols during all the seasons in the south-westerly direction (Fig. S3) which were previously studied
331 by Stieger et al., (2018). However, it is known that the AMS technology cannot properly detect sea salt (Huang et al., 2018;
332 Ovadnevaite et al., 2014) because the majority of chloride is in the refractory part which cannot be flash vaporized at 600°C .
333 Consequently, the chloride detected by the ACSM is mostly related to combustion processes (wood, coal combustion as well
334 as trash burning; Li et al., 2012).

335 **3.1.2 eBC- PM_1 and organics**

336 The eBC- PM_1 showed its maximum mass concentration and mass fraction to PM mass during winter time at $1.38 \mu\text{g}/\text{m}^3$ and
337 9 %, respectively (Fig. 2), and only $0.25 \mu\text{g}/\text{m}^3$ and 4 %, respectively, during summer time (Fig. 2). This is consistent with the
338 expected highest anthropogenic emissions from fossil fuel consumption (house heating and energy productions) in winter
339 compared to summer (Spindler et al., 2010). Furthermore, considering measured eBC- PM_1 in regard to wind speed and wind
340 direction from NWR plots (Fig. S3), eBC- PM_1 presented transported and local emissions. The highest mass concentrations for
341 fall, winter, and spring seasons could be linked to north-easterly and south-westerly winds with higher wind speed (above 10
342 m/s). While in summer time it is mostly linked to the surrounding emissions regardless of wind direction with lower wind
343 speed (Fig. S3). Significant changes in the diurnal profiles of eBC- PM_1 for the different seasons can be found with the highest
344 mass concentrations throughout the cold months compared to warm months owing to house heating (Fig. 3). It also showed
345 morning and evening peaks during all seasons (Fig. 3). This is consistent with those observed for the nitrogen oxides (Fig. S4),
346 which might be attributed to liquid fuel emissions and possibly the impact of the traffic rush hours on the main street, B 87,
347 located approximately 1 or 1.5 km north of the station, (Yuan et al., 2021). In the following chapter, diurnal patterns showed
348 lower mass concentrations at noon, and increased in the late afternoon to become nearly constant from 8 p.m. until midnight
349 (Fig. 3). This ambient particulate pollution resulting from very surrounding sources in the village was reported by van Pinxteren
350 et al., (2020). Diurnal increments of eBC- PM_1 were smaller in fall and spring compared to winter; the increment in summer is
351 also correspondingly low due to the absence of house heating emissions, and the diurnal variation in the increment is
352 determined by surrounding motor vehicle emissions in combination with the mixing layer height (van Pinxteren et al., 2020).
353 Further discussions on the seasonal trend of the eBC- PM_1 can be found in Sect. 3.3.

354

355 Organic aerosol (OA) was the predominant species throughout the whole year, with a mean mass concentration of $4.84 \mu\text{g}/\text{m}^3$
356 and a mass fraction of 46 % (Fig. 1c; Table. 1). The OA mass fraction decreased from the maximum value in summer and
357 attained a minimum mass fraction in winter (58 %, 39 %, respectively; Fig. 2b). Similar to the comparison of previous inorganic
358 AMS measurements performed at Melpitz (Poulain et al., 2011), AMS-OA contribution to total PM_{10} showed maximum
359 contribution during summer (59 %, Table. S1), and minimum contribution during winter (23 %) as well. However, the mass
360 concentration of OA increased from its lowest value in summer and reached its highest value in winter time ($3.67 \mu\text{g}/\text{m}^3$, 6.21
361 $\mu\text{g}/\text{m}^3$ respectively; Fig. 2, Table. 1). Similar to eBC- PM_{10} , by analyzing NWR plots, OA measured according to wind direction
362 and wind speed showed the highest average mass concentrations for north-easterly and south-westerly winds in winter (Fig.
363 S3). In fall, polluted air masses came from the north-easterly direction, and in spring and summer OA, surrounding emissions
364 closer to Melpitz were identified (Fig. S3). The diurnal cycle of the organic had an identical pattern across all seasons (Fig. 3),
365 showing the highest mass concentration in night time, a small peak in the early hours of the morning related to rush hours, and
366 the lowest mass concentrations around the early afternoon. The peak observed around 12:00 UTC in summer time (Fig.3) can
367 be due to the local photochemical production that leads to the formation of secondary organic aerosol mass during the day,
368 similar to the diurnal behavior of sulphate (previously discussed in Sect. 3.1.1). However, the reduction in total OA mass
369 concentration throughout the day (Fig. 3), which was mostly observed during the warm seasons (spring and summer), could
370 be clearly related to the dilution effect of increasing mixed layer height. During warm days, evaporation of semi-volatile
371 organics from the particle phase cannot be completely excluded (Schaap et al., 2004; Keck and Wittmaack, 2005). In
372 comparison between Bressi et al., (2021) and the current study for Melpitz station, the daily variation of organic are similar in
373 both winter and summer seasons, while there are differences between Melpitz with other rural-background stations due to the
374 different geographical location and meteorological conditions (Bressi et al., 2021).

375

376 Overall, eBC- PM_{10} and OA can be composed of various sources with strong seasonal dependencies, as well as be influenced
377 by different responses to atmospheric dynamics depending on meteorological parameters, geographical locations, and chemical
378 processes. Therefore, a comprehensive analysis of the OA and eBC- PM_{10} sources was performed using source apportionment
379 techniques.

380 **3.2 Source apportionment of OA**

381 The chosen solution for the organic aerosol source apportionment contained five different factors based on their time series
382 and mass spectra (Fig. 4). The source apportionment solution is based on a partly constrained rolling approach with three
383 primary organic factors (POA), namely HOA (on average $0.30 \mu\text{g}/\text{m}^3$ and 6 % of the total OA; Table.1 and Fig. 4), BBOA (on
384 average $0.39 \mu\text{g}/\text{m}^3$ and 7.9 % of the total OA) and CCOA (on average $0.77 \mu\text{g}/\text{m}^3$ and 15.4 % of the total OA). In addition to
385 these POA factors, two oxygenated organic aerosols (OOAs) were identified as LO-OOA (on average $1.62 \mu\text{g}/\text{m}^3$ and 32.4 %
386 of the total OA), and MO-OOA (on average $1.92 \mu\text{g}/\text{m}^3$ and 38.4 % of the OA). The seasonal average mass concentrations and

387 relative mass fractions of each OA factor to the total OA mass and their seasonal diurnal variation are presented in Figures 5
388 and 6; respectively. They will be discussed separately in the following sections.

389 3.2.1 POA factors

390 The HOA mass spectrum (Fig. 4b) is recognized by mass fragments at unsaturated and saturated hydrocarbon chain pairs m/z
391 41 (C_3H_5), 43 (C_3H_7), m/z 55 (C_4H_7) and 57 (C_4H_9) (Zhang et al., 2005; Canagaratna et al., 2004), which are representative of
392 liquid fuel combustion emissions and are associated with either traffic emissions or domestic heating fuel (Wang et al., 2020).
393 This result designates HOA as a minimal source of OA at the monitoring site, which is consistent with previous studies in the
394 PM_{10} range made in the same place: a) total average was 7 % of the organic mass concentration in a study by Crippa et al.,
395 (2014) total average was 3 % of PM_{10} size range between 0.05-1.2 μm mass concentration in a study by van Pinxteren et al.,
396 (2016) (Table. S3). However, in comparison with other ACSM/AMS stations in Europe (22 stations; Chen et al., 2022),
397 Kosetice with 9.7 % as a rural-background site, and Bucharest with 13.7 % as an urban-background site showed the minimum
398 annual HOA mean contribution of total OA, which is similar to the contribution at Melpitz.

399 Mass concentration of HOA followed a slightly increasing seasonal pattern towards the cold months, from 0.23 $\mu g/m^3$ in
400 summer to 0.36 $\mu g/m^3$ in the winter (Fig. 5a; Table. 1). HOA presented a low correlation with nitrogen oxides over the entire
401 period ($R^2=0.17$, Table. 1), but it correlated well with eBC- PM_{10} in winter ($R^2=0.52$; Table. 1) and showed a weaker correlation
402 in summer ($R^2=0.28$; Table. 1). Possibly HOA is also associated with household heating (35 % by oil and 11 % by liquid
403 petroleum gas, van Pinxteren et al., 2020) rather than traffic emissions, especially during the cold months. Analyzing the NWR
404 plots demonstrates the highest HOA mass concentration was observed at low wind speed during the warm period (Fig. 7)
405 indicating, rather local emission sources. While during the cold period a clear increase of the mass concentration can be
406 associated with the highest wind speed (> 10 m/s) mostly coming from the North to East sector. During periods with wind
407 speeds below 10 m/s, the two dominant wind sectors (NE and SW) can be observed. The first one might be associated with
408 emission plumes coming from either the surrounding traffic emissions (the federal street B 87), as well as the domestic
409 emissions are associated not with house heating in summer but with hot water production (van Pinxteren et al., 2020), as well
410 as the city of Torgau (with approx. 20,000 inhabitants, distance from 7 km). Although the SW sector shows a lower HOA mass
411 concentration in comparison to the NE one, it corresponds to the direction of the city of Leipzig (above 600 000 inhabitants,
412 approx. 50 km). Therefore, it might be associated with the influence of the pollution plume of the city of Leipzig.

413 The diurnal patterns of HOA reproduced two peaks in the morning and evening for all seasons (Fig. 6), which is related to
414 traffic rush hours and linked to surrounding emissions from the main street (B 87, approx. 1.5 km north of the station), Melpitz
415 village itself, and emissions coming from Leipzig and Torgau residential areas. The small time shift for the start of the evening
416 increase corresponds to the time shift of the sunrise between winter and summer. The diurnal cycles reached a systematic
417 minimum during the day time probably not only owing to emission decrease but also emphasizing the effect of dynamic
418 atmospheric processes (e.g. mixing layer height (MLH) and planetary boundary layer (PBL)) (Fig. 6, and S4). Oppositely to
419 what can be seen during the day time, night time mass concentrations appeared to be unaffected by the seasons, showing

420 similar mass concentrations all year round, i.e. their mass concentration rose continuously in the early evening and remained
421 at a very similar mass concentration over the night, which supports the hypothesis of yearlong continuous rather surrounding
422 emissions. Nevertheless, the differences between HOA mass concentration during the night time from summer to winter season
423 (Fig. 6) are small and can be covered by the uncertainties of PMF result ($\pm 32.5\%$, Fig. S2), however, it can be explained by
424 different emission sources, condensation of POA (Chen et al., 2022), evaporation, oxidation processes (Saha, et al., 2018), and
425 potential night time aging process by high ozone concentration (Kodros, et al., 2020).

426

427 The mass spectra of BBOA are identified by ions at m/z 29, 43, 60, and 73 (Fig. 4b), known as fragments tracers of anhydro-
428 sugars like levoglucosan (Alfarra et al., 2007), which have been recognized as indicators of wood combustion processes
429 (Simoneit et al., 1999; Simoneit and Elias, 2001). This is confirmed by the correlation between BBOA and levoglucosan over
430 the whole period ($R^2=0.65$; Table. 1). On average, BBOA mass concentration and contribution were $0.39\ \mu\text{g}/\text{m}^3$ and 7.9% ,
431 respectively (Table. 1 and Fig. 4a). However, its contribution is highest during winter time (10.6% ; Fig. 5), which is similar
432 to previous studies in different PM ranges for the Melpitz station during the cold months: a) in PM_1 range, 14% of OA mass
433 concentration in fall (Crippa et al., 2014); b) in $0.05\text{-}1.2\ \mu\text{m}$ range, highest contribution with 10% of PM mass concentration
434 in winter (van Pinxteren et al., 2016); and c) in PM_{10} range, highest contribution with 16% of PM mass concentration in winter
435 (van Pinxteren et al., 2020).

436 By analyzing the NWR model, the high mass concentration of BBOA in cold months, regardless of wind speed can be observed
437 with two wind sectors coming from north-east and south-west directions. These BBOA emissions are mainly attributed to
438 residential heating in Melpitz village and also indicate the effect of transported biomass burning emissions to the sampling site
439 with higher wind speed ($> 10\ \text{m/s}$, Fig. 7). While in summer time, it is still observable as surrounding emissions during periods
440 of low wind speed (Fig. 7 and Fig. S4) with a mass concentration of $0.21\ \mu\text{g}/\text{m}^3$ and a contribution of 6.1% to total OA (Fig.
441 5). The presence of BBOA in the summer can be linked to water heating systems using wood briquettes and logs (estimated at
442 32% of total central heating in this area, van Pinxteren et al., 2020). Moreover, it can also be related to recreational open fires
443 and/or barbecue activities (van Pinxteren et al., 2020). This result is similar to other ACSM/AMS rural-background stations in
444 Europe (22 stations; Chen et al., 2022); both Magadino and Kosetice showed the highest contribution of BBOA during winter
445 time (27.4% and 15.5% respectively).

446 The diurnal cycles, peaking from early evening to early morning in winter (Fig. 6), match the expectations for a factor related
447 to domestic heating activities, along with a better eBC- PM_1 correlation during winter than during summer time ($R^2=0.81$, and
448 $R^2=0.42$, respectively; Table. 1). Finally, in opposition to HOA, the night time BBOA mass concentration showed a strong
449 seasonal variation, having its highest mass concentration during winter nights and lowest during summer time, the influence
450 of the impact of house heating emissions on the BBOA emissions. However, the day time behavior reflects the influence of
451 enhanced vertical mixing during day time (higher temperature, Fig. S4) combined with high wind speeds can readily cause
452 dilution and thus low pollutant concentrations near the ground (Chen et al., 2021; Via et al., 2020; Paglione et al., 2020).

453

454 The mass spectrum of CCOA is characterized by fragments at m/z 77, 91, and 115 (Fig. 4b) as previously reported by Dall'Osto
455 et al., (2013); Xu et al., (2020); Tobler et al., (2021) and Chen et al., (2022). These specific fragments can be associated with
456 unsaturated hydrocarbons, particularly ion peaks related to polycyclic aromatic hydrocarbon (PAH). The CCOA time series
457 showed the strongest correlation with eBC-PM₁ ($R^2= 0.9$; Table. 1). In addition, several studies reported that coal combustion
458 emissions are often accompanied by high chloride mass concentrations (e.g; Iapalucci et al., 1969; Yudovich and Ketris, 2006
459 and Tobler et al., 2021). Here, the correlation between CCOA and chloride was higher during winter than during summer time
460 ($R^2= 0.41, 0.15$ respectively; Table. 1), as the gas-particle phase equilibrium dramatically changes with rising temperatures
461 (Tobler et al., 2021). Although chloride is almost observable in the particle phase as ammonium chloride (NH₄Cl) at lower
462 temperatures, chloride is typically observable in the gas phase as hydrogen chloride (HCl) at higher temperatures (Tobler et
463 al., 2021).

464 CCOA represented on average 15.4 % of the total OA ($0.77 \mu\text{g m}^{-3}$), (Table. 1; Fig. 4a) and is the most important POA over
465 the entire period. No CCOA factor was identified in the previous AMS measurements made at Melpitz (Crippa et al., 2014).
466 Most likely this factor was not properly resolved and/or it was not possible to properly separate it from the other factors since
467 no reference mass spectra for CCOA were reported in the literature at that time. CCOA showed the highest mass concentration
468 and mass fraction during the winter ($1.58 \mu\text{g/m}^3$, 23 %, respectively; Fig. 5a; Table. 1). By analyzing the NWR plots, this high
469 mass concentration during winter time can be related to the surrounding emissions and long-range transported air masses
470 coming from two different directions, north-easterly and south-westerly (Fig. 7). Not surprisingly, the lowest mass
471 concentration and contribution were observed during the summer time ($0.30 \mu\text{g/m}^3$, 8.7 %, respectively; Fig. 5a; Table. 1),
472 which most probably correspond to only long-range transport as later discussed in Sect. 3.4 (Fig. 9). Moreover, this result is
473 consistent with previous measurements made in the same place. For the size range 0.05-1.2 μm van Pinxteren et al., (2016)
474 reported a contribution of 29 % and 21 % of the PM in winter and summer respectively, and a contribution of 7 % and 0 % for
475 winter and summer respectively for the PM₁₀ range was found (van Pinxteren et al., 2020). From all ACSM/AMS stations (22
476 stations; Chen et al., 2022) only Melpitz as a rural-background site and Krakow as an urban-background site showed the coal
477 combustion emissions with the maximum contribution during winter for both sites (Krakow: 18.2 % and Melpitz: 23 %)
478 compared to summer (Krakow: 4.5 % and Melpitz: 8.7%). The drastic seasonal changes in Krakow are attributed to the
479 common use of coal burning for residential heating reasons during the winter time (Tobler et al., 2021), while in Melpitz, as
480 discussed above, coal combustion is affected by both surrounding and transported emissions from other sites. Mass
481 concentrations of CCOA during night time were much higher than during day time throughout all seasons (Fig. 6), further
482 verifying the increased coal combustion emissions from coal heat generation at night in winter time and the potential decrease
483 in emissions during the day due to a strong influence of atmospheric dynamics.

484 3.2.2 OOA factors

485 The two OOAs (Fig. 4) referred to as LO-OOA and MO-OOA are known to be characterized by the different ratios of their
486 m/z 43 and m/z 44 fragments (Fig. 4b), which represent the oxidation level (Canagaratna et al., 2015). While m/z 43 could be

487 derived from $C_2H_3O^+$ (a signature of the semi-volatile) and/or $C_3H_7^+$ (a signature of the primary emissions of the hydrocarbon-
488 like), m/z 44 is mainly derived from the fragment of CO_2^+ (a signature of oxygenated, particularly acids) (Canonaco et al.,
489 2015; Ng et al., 2010). As presented in Fig. 4b, MO-OOA mass spectra showed a notable peak at m/z 44. This spectrum has
490 been extensively recognized as low volatility OOA (LV-OOA) and described to be made-up of aged secondary OA (SOA) and
491 highly oxidized OA (Ulbrich et al., 2009; Zhang et al., 2011; Ng et al., 2011); while the mass spectra of LO-OOA in this study
492 presented a higher m/z 43 (Figs. 4b) compared to MO-OOA, which is similar to the mass spectral pattern of the previously
493 reported freshly formed semi-volatile OOA (SV-OOA) (Jimenez et al., 2009; Ng et al., 2010). To differentiate the variations
494 of the OOAs factor, the f_{44} vs f_{43} space was used which is a typical diagnostic tool based on atmospheric aging (Ng et al.,
495 2010).

496 The seasonal f_{44}/f_{43} for OOAs measured points and the f_{44}/f_{43} for modelled factor profiles (LO-OOA and MO-OOA) are
497 presented in Fig. S5. The data points in Fig. S5 are distributed differently according to the season (Chen et al., 2021; Canonaco
498 et al., 2015; Crippa et al., 2014; Chazeau et al., 2022). Furthermore, the modelled factor profile points represent a high
499 variability in space, especially for LO-OOA. This assumes how an annual or seasonal PMF solution, unless a larger number
500 of factors are used, would perform poorly in capturing all of the variations of SOA. In order to capture time-dependent changes,
501 in particular for LO-OOA, it is, therefore, advantageous to perform rolling PMF analysis. The triangle plot defined by Ng et
502 al. (2010) is also shown in Fig. S5. As assumed the LO-OOA points were concentrated in the lower part of the space, whereas
503 more aged MO-OOA points relocated to the upper part of the space during the aging process. The fall, spring, and summer
504 data points were all located on the right side of the triangle (Fig. S5), however, the winter data points were located near the
505 top and inside the triangle. The data points on the right side of the triangle correspond to the time exposed to higher
506 temperatures more than those that are within the triangle. This could be attributed to an increase in biogenic SOA emissions if
507 the temperature increased, as biogenic OOA appears to be dispersed all along the right side of the triangle. Furthermore, as the
508 temperature is reduced, the increased biomass emissions cause the OOA points to lie vertically inside the triangle, as seen in
509 the winter data.

510

511 The two OOAs were the two most significant contributors to the total OA fraction (Fig. 4) over the entire period. The seasonal
512 mean mass concentrations of MO-OOA varied from higher mass concentrations during winter ($2.25 \mu\text{g}/\text{m}^3$) and lower during
513 summer time ($1.44 \mu\text{g}/\text{m}^3$, Table. 1). However, the highest MO-OOA mass concentrations found during the cold periods are
514 similar to the seasonal patterns in POA. This high mass concentration in cold seasons can be seen from the NWR plot (Fig. 7)
515 presenting local emissions with low wind speed ($> 5 \text{ m/s}$) and transported emissions from east, north-east, and south-west
516 directions with high wind speed ($< 5 \text{ m/s}$). Furthermore, high mass concentrations of MO-OOA are generally found at high
517 relative humidity ($\text{RH} > 80 \%$) and low temperature ($< 0 \text{ }^\circ\text{C}$), i.e., conditions during winter time (Fig. S6). This low air
518 temperature condition can be linked to a possible scenario for an increase in the MO-OOA precursor emissions from biomass
519 burning and coal combustion as a result of residential heating activities during winter time. Therefore, significant enhancement
520 appears to be an effect of RH during winter, proposing that the aqueous-phase heterogeneous mechanisms could also play a

521 crucial way in the regional MO-OOA formation through winter as suggested by Gilardoni et al., (2016). In contrast, no RH-
522 temperature-dependent trends for the MO-OOA were found in the other seasons (Fig. S6), indicating more complex formation
523 processes during other seasons. Meanwhile, MO-OOA diurnal cycles presented a seasonal variation as well, with a remarkable
524 enhancement in the evening and night time during winter (Fig. 6), indicating a potential regional formation mechanism
525 containing night time chemistry (Tiitta et al., 2016), and descending pattern from night time to day time due to planetary
526 boundary layer effect. While in fall, spring, and summer, MO-OOA displayed a considerable increase during the day (Fig. 6),
527 indicating that higher temperatures result in considerable regional photochemical production of SOA particles (Fig. S4) and
528 enhanced solar radiation (Petit et al., 2015). Furthermore, regarding the correlation of mass concentration of MO-OOA with
529 sulphate, the latter is regarded as a local secondary production indicator (Petit et al., 2015, and Table. 1). Consequently,
530 alongside almost stable mass spectra throughout the year, MO-OOA seems to be derived from a variety of seasonal-dependent
531 formation mechanisms and sources (such as aged background, biomass burning, coal combustion, and biogenic sources).

532

533 The seasonal mean mass concentrations of LO-OOA varied from higher mass concentrations during fall ($2.13 \mu\text{g}/\text{m}^3$) and
534 lower mass concentrations during spring time ($1.24 \mu\text{g}/\text{m}^3$, Table. 1). Temperature had a significant effect on LO-OOA, and
535 showed a distinguishable seasonal variation pattern. The temperature-RH dependence of the LO-OOA was not quite similar
536 depending on the season (Fig. S6). The highest winter time LO-OOA mass concentrations were found mostly at low
537 temperatures and high RH environments, indicating that gas-particle partitioning might have a key role in LO-OOA formation
538 throughout this season. The freshly formed SOA deriving from primary biomass burning and coal combustion emissions, as
539 found in previous studies (Crippa et al., 2013; Zhang et al., 2015; Y. Sun et al., 2018; Stavroulas et al., 2019) can also affect
540 the LO-OOA during the cold months. Furthermore, since nitrate could be originated locally or arrived from a long distance to
541 Melpitz (Sect. 3.1.1), with a good correlation between LO-OOA and nitrate ($R^2= 0.59$) during winter, the long-range
542 transported LO-OOA from different directions reaching to measuring site could be explained (Fig. 7). Different LO-OOA
543 daily cycles were also found in different seasons (Fig. 6). The daily changes in LO-OOA displayed higher mass concentrations
544 in night time compared to day time in fall, spring, and summer (Fig. 6), highlighting the significant roles of night time chemistry
545 and/or gas-particle partitioning in the LO-OOA formation; while the decrease during the day is partly linked to the atmospheric
546 dilution effect (Fig. S4), evaporation and photochemical aging into MO-OOA (Fig. 6). For winter night increments, lower
547 temperature in favor of condensation; and more abundant precursors present considering increased BBOA emission, therefore
548 enhanced night-chemistry activities, leads to higher LO-OOA; moreover, shallow boundary layer in winter and night time
549 inversion caused pollutants to accumulate.

550 **3.3 Source apportionment of eBC-PM₁**

551 By applying a multilinear regression model, during the source apportionment analysis, eBC-PM₁ correlated with every one of
552 the three identified primary organic factors (HOA, BBOA, and CCOA, Table. 1). CCOA appeared to be the largest source of
553 eBC-PM₁, contributing half of it (eBC-PM₁-CCOA 55 %, Table. 1), followed by eBC-PM₁ associated with BBOA 37 % (eBC-

554 PM₁-BBOA), while the lowest contribution was found for eBC-PM₁-HOA (8 %). However, the contribution of sources to the
555 total eBC-PM₁ strongly depends on the season. Looking at each individual source, the hydrocarbon-like emissions contributed
556 most to the eBC-PM₁ fraction in the fall (eBC-PM₁-HOA with 22 %, Table. 1; Fig. 8b), while biomass burning emissions
557 dominated the eBC-PM₁ in summer and coal combustion emission dominated in winter (eBC-PM₁-BBOA and eBC-PM₁-
558 CCOA with 69 % and 56 %, Table. 1). In the diurnal cycle, contribution to the total eBC-PM₁ of eBC-PM₁-HOA showed two
559 peaks in the morning and evening for fall, spring, and summer (Fig. S7), reflecting the impact of the traffic rush hours as
560 mentioned in Sect. 3.2.1, and the minimum contributions during the day time due to the effect of lowest emissions and PBL
561 effect (Fig. S4). However, winter time did not show a strong variation in the diurnal cycle (Fig. S7). This indicates the potential
562 influence of continuous emissions at the measurement site. Biomass burning combustion with its maximum contribution during
563 the day in summer (Fig. S7) can be related to a variety of different eBC-PM₁-POA mass concentrations (Fig. S7b), while the
564 BBOA mass concentration was almost constant, the other POA mass concentration decreased during the day. Coal combustion
565 showed an increasing contribution during night time in all the seasons (Fig. S7), especially during the winter time, which
566 further confirms the enhanced coal combustion emission in winter nights (Fig. S7b).

567 **3.4 Seasonal air mass clustering**

568 As mentioned before, the geographical origin of the PM₁ chemical species and also PMF components are not only emitted
569 from the surrounding area but also transported. Therefore, to better identify the origin of their sources, trajectory analysis, and
570 their clustering analysis were applied using the self-developed back-trajectory cluster method (BCLM) (Sun et al., 2020; Ma
571 et al., 2014; Hussein et al., 2006). Regarding this cluster approach, six air masses were identified at Melpitz station for the
572 winter season, four air masses for the transition seasons, and five air masses for the summer season (Fig. 9a). The number of
573 clusters with their corresponding mean mass concentration of PM₁ chemical species and PMF factors of organics are
574 summarized in Table. 2 and with more details in Tables S4 and S5.

575 **3.4.1 Winter**

576 Fig. 9b and 9c illustrate the mass concentration and contribution of PM₁ chemical species and PMF factors of organic for each
577 air mass type at Melpitz based on the type of air masses. For the winter season, the cluster CS-ST corresponds to more
578 surrounding emission origin with a PM mean value of 21.95 µg/m³, which occurred during 14 % of the total measurement
579 period. These surrounding emissions refer to the emissions from Melpitz station directly, Melpitz village, and short distance
580 transported particles like particles from Leipzig and Torgau. This cluster presented the highest mass concentration of LO-OOA
581 to the PM mass (2.73 µg/m³). In fact, SOA is considered to be formed by biomass burning as well as coal combustion,
582 particularly during the winter when biogenic emissions and UV radiation are low (Lanz et al., 2010; Kodros, et al., 2020). In
583 this condition and in the presence of NO₂ and O₃, the biomass burning emissions could age rapidly and produce SOA. In
584 conclusion, this cluster could confirm the role of freshly formed SOA which originated from the primary biomass burning and
585 coal combustion emission (mass concentrations of 0.97 µg/m³ and 1.89 µg/m³, respectively). Furthermore, nitrate showed a

586 high mass concentration and contribution in this air mass ($5.38 \mu\text{g}/\text{m}^3$ and 25 %, respectively) due to e.g., meteorological
587 conditions and abundant precursors.

588 The cluster CS-A1 with the highest mass concentration of PM ($29.14 \mu\text{g}/\text{m}^3$) represented Eastern European continental air
589 masses (passing Poland and the Czech Republic) during anticyclonic flow which occurred during 18 % of the total
590 measurement period, meaning that Melpitz was under their influence during winter. This air mass, with the highest POA mass
591 concentration ($5.56 \mu\text{g}/\text{m}^3$), especially coal combustion emissions (CCOA and eBC-PM₁-CCOA with an average mass
592 concentration of $4.01 \mu\text{g}/\text{m}^3$ and $1.93 \mu\text{g}/\text{m}^3$, respectively), highlight the importance of long-range transported emissions. This
593 cluster also contained the highest mass concentration of sulphate ($5.39 \mu\text{g}/\text{m}^3$) and could support the importance of coal
594 combustion on sulphate formation, which is known to be strongly emitted by coal power plants (Wierońska-Wiśniewska et al.,
595 2022).

596 The air mass CS-A2 identified as marine-influenced air mass with a mean value of $13.39 \mu\text{g}/\text{m}^3$ of PM came from the United
597 Kingdom with the anticyclonic flow, which occurred during 8 % of the total measurement period. This cluster presented a low
598 mass concentration of POA and for two OOAs almost the same mass concentration and contribution (Table. S5 and Table.
599 S6). Since Melpitz is placed away from the coast, therefore the sampling location is affected by aged maritime air masses
600 (Poulain et al., 2011). Inorganics are dominated by nitrate in this cluster with the high mass concentration ($3.86 \mu\text{g}/\text{m}^3$) which
601 represents the highest mass fraction (50 % of the total inorganic species).

602 The CS-C1 air mass with a mean value of $15.99 \mu\text{g}/\text{m}^3$ characteristic of Southern European air mass, came from an industrial
603 and polluted area starting from Spain and partly crossing Italy with the cyclonic flow, which occurred during 10 % of the total
604 measurement period. POA mass concentration and contribution were low in this cluster, while SOA, especially MO-OOA,
605 showed the highest mass concentration of PM over the entire period ($3.77 \mu\text{g}/\text{m}^3$) and the highest contribution during the winter
606 season (24 %). This can be linked to the high sulphate in this air mass ($2.99 \mu\text{g}/\text{m}^3$), which showed that the regional influence
607 by contribution from aged BBOA and CCOA might be manifested in MO-OOA (as discussed in Sect. 3.2.2).

608 Finally, CS-C2a and CS-C2b were both associated with cyclonic and marine influence conditions which only occurred for a
609 short time (3 % and 2 % of the total measurements, respectively), showing the lowest PM mean value ($4.09 \mu\text{g}/\text{m}^3$ and 2.60
610 $\mu\text{g}/\text{m}^3$, respectively). Both of them showed almost the same mass concentration and contribution of POA (Fig. 8a and b; and
611 Table. S5 and S6). However, similar to CS-A2, cluster CS-C2a contained a marine component at the beginning point of the
612 air masses, and in the following time it was dominated by continental areas (France and southern Germany), where due to the
613 longer time transferring over continent and aging process, it showed more nitrate mass concentration and contribution than
614 CS-C2b ($1.35 \mu\text{g}/\text{m}^3$, $16 \mu\text{g}/\text{m}^3$; and 28 % 14 %, respectively). Whereas CS-C2b started near Iceland with same history of the
615 air mass over the continent, and in comparison, with CS-C2a, it presented a higher contribution of sulphate (29 % and 19 %,
616 respectively), which could be associated with aged marine air mass due to the higher contribution of MO-OOA (21 % and 18
617 %, respectively).

618 3.4.2 Transition seasons

619 For transition seasons (fall and spring), whereas the four clusters showed quite similar PM mass concentrations (Fig. 9) which
620 might be linked to the overall weather situation during these two times of the year, their chemical composition strongly
621 depended on their origins. TS-A1 and TS-A2 corresponded to two different types of anticyclonic air masses with respective
622 mean PM mass concentrations of $6.06 \mu\text{g}/\text{m}^3$ and $5.86 \mu\text{g}/\text{m}^3$. Cluster TS-A1 which occurred during 4 % of the total
623 measurements period, started from Finland, crossing the Estonian, Latvian, Lithuanian, and Polish coasts before arriving at
624 Melpitz. Although it might contain a certain marine component, this cluster mostly followed coastal areas, which means that
625 in this cluster OA mass concentration dominated PM ($2.95 \mu\text{g}/\text{m}^3$). Furthermore, this cluster showed continental and polluted
626 aspects with the highest LO-OOA mass concentration and contribution during transition seasons ($1.03 \mu\text{g}/\text{m}^3$ and 17 %
627 respectively), which is linked to originating from freshly formed SOA from primary biomass burning and coal combustion
628 emissions around coastal areas. On the other hand, cluster TS-A2 (4 % of the measurement period) is characterized as a marine
629 cluster and started from the south of Iceland/Greenland. This cluster showed inorganics as the dominant components in PM
630 with a high mass concentration and a mass fraction ($3.35 \mu\text{g}/\text{m}^3$ and 58 % respectively). Since Melpitz is influenced by aged
631 marine air masses, this cluster showed a maximum nitrate mass concentration during the transition seasons ($1.54 \mu\text{g}/\text{m}^3$ and a
632 contribution of 26 %, respectively).

633 Finally, two other clusters TS-C1 and TS-C2 were two different types of cyclonic air masses in fall and spring time, with mean
634 PM mass concentrations of $4.69 \mu\text{g}/\text{m}^3$ and $4.94 \mu\text{g}/\text{m}^3$ respectively. These trajectories with different types of marine influenced
635 air masses occurred for a very short period of time (3 % and 4 % of the total measurements period, respectively). The first one,
636 TS-C1, started from the Atlantic Ocean near Spain and is associated with a more continental influence, which is why organic
637 mass concentration and contribution were higher than inorganics. However, The LO-OOA contribution of this cluster was the
638 highest during this time period (26 %) due to the aging processes of primary organic aerosols especially CCOA, which had a
639 maximum mass concentration ($0.31 \mu\text{g}/\text{m}^3$ and mass fraction of 7 %, respectively). While the second one, TS-C2, was almost
640 a pure marine cluster, coming from the Norwegian Sea. In opposition to TS-C1, PM was dominated by inorganics in TS-C2,
641 with a high mass concentration of nitrate ($1.35 \mu\text{g}/\text{m}^3$) representing the aging effect due to the long-time transfer over the
642 continents.

643 3.4.3 Summer

644 During the summer season, the different clusters showed strong changes in both chemical compositions and total mass
645 concentrations. Cluster WS-ST was identified as the local air mass with a mean value of $8.97 \mu\text{g}/\text{m}^3$, which occurred for a
646 short period, 6 % of the measurement. However, this cluster contained a low POA mass concentration but a maximum
647 contribution of MO-OOA (32 %), assuming important regional photochemical roles of SOA particles with higher temperatures
648 (Fig. S4) and enhanced solar radiation (Petit et al., 2015).

649 Air masses WS-A1 and WS-A2 were two different types of anticyclonic air masses with different directions and different
650 mean PM mass concentrations. Cluster WS-A1, known as the highest mass concentration during summer time, ($16.95 \mu\text{g}/\text{m}^3$
651 and contribution of 11 % of the measurement period) was the continental air mass which was coming from Eastern Europe
652 during the anticyclonic flow (starting from Belarus, crossing Poland and the Czech Republic). This air mass included maximum
653 inorganics and organics especially CCOA mass concentration ($1.28 \mu\text{g}/\text{m}^3$) during summer time, which can explain the existing
654 higher CCOA during summer, and showed the role of long-range transported emissions in the summer season. However, WS-
655 A2 air mass, with a mean value of $9.48 \mu\text{g}/\text{m}^3$ was a marine-influenced air mass and was coming from the North Sea, which
656 only occurred for a short period (6 % of the total measurement period).

657 Moreover, two cyclonic air masses, WS-C1 and WS-C2, were also identified as two different marine clusters. These trajectories
658 did not occur very often, only 5 % and 3 % of the total measurement period, respectively. The starting point of WS-C1 with a
659 mean value of $8.41 \mu\text{g}/\text{m}^3$ was the Celtic Sea, but in the following time, it predominantly passed over continental areas (France
660 and southern Germany), which means it could be aged and the result can be shown in the high mass concentration of nitrate
661 and sulphate in this cluster ($1.63 \mu\text{g}/\text{m}^3$ and $1.86 \mu\text{g}/\text{m}^3$, respectively). Finally, the starting point of WS-C2 with a mean value
662 of $4.46 \mu\text{g}/\text{m}^3$, was near Iceland, with the lowest PM mass concentration during summer. However, it showed the highest
663 sulphate contribution (27 %) at this time which could be associated with aged marine air mass like other marine air masses.

664 **3.4.4 Cluster seasonality**

665 A parallel comparison can be made between the winter and summer clusters. Clusters CS-A1 and WS-A1 both show the
666 highest POA contribution dominated by coal combustion, which emphasizes that the origin of this source could be associated
667 with the transport of the coal power plants emissions from Eastern Europe (e.g. Eastern part of Germany, Poland, Czech
668 Republic and further countries located in the East). These clusters were not only affected by the winter air quality but also the
669 summer air quality.

670 Clusters CS-ST and WS-ST, which were known as local air masses, showed the seasonal effect on the chemical component.
671 First, the volatility of ammonium nitrate at higher summer temperatures could explain their lower value in summer. Then,
672 atmospheric photochemical oxidation processes affected the sulphate locally formed emission in summer, which its highest
673 value over inorganic components during summer can be confirmed. Not surprisingly, due to the residential heating effect, POA
674 mass concentration was very high during winter; however, freshly formed SOA originating from biomass and coal emissions
675 can explain the higher LO-OOA mass concentration in winter.

676 During the whole period, some marine air masses with cyclonic and anticyclonic flow showed the important roles of aged
677 marine air masses over the measurement site: a) clusters CS-A2 and WS-A2 with anticyclonic pattern starting from the North
678 and/or Norwegian Sea, and b) CS-C2a, WS-C1, and TS-C1 starting from the Celtic Sea near Spain, and also CS-C2b and WS-
679 C2 starting from Iceland, all with cyclonic patterns contain nitrate and sulphate during the transferring over the continental
680 areas in different seasons.

681 4 Conclusion

682 The chemical compositions of non-refractory fine aerosol (NR-PM₁) at the German rural-background observatory Melpitz
683 were investigated in this study over a one-year period between September 2016 and August 2017. Overall, the averaged total
684 PM₁ mass concentration is 10.49 µg/m³ and follows a clear seasonal pattern, with the highest mass concentration during winter
685 (15.95 µg/m³) and the lowest mass concentration during summer time (6.24 µg/m³). The organic aerosol was the most
686 significant component, accounting for 46% of total PM₁ and showing significant seasonal dependency (39 % in winter to 58
687 % in summer). It was followed by sulphate (15 % and 20 %) and nitrate (24 % and 11 %). For OA source apportionment, PMF
688 in a rolling fashion has been applied using the SoFi Pro, which provided the decomposition of time-dependent factor profiles
689 that were able to better capture the variability of OA sources across seasons in comparison with the conventional seasonal
690 PMF. The final solution enabled the identification of five factors throughout the one-year measurements of OA; HOA, BBOA,
691 CCOA, LO-OOA, and MO-OOA. Using the correlation between HOA, BBOA, and CCOA with eBC-PM₁, a multilinear
692 regression approach was applied to perform the source apportionment of eBC-PM₁.

693 Generally, in Melpitz, HOA as a minor source of OA (6 % of the contribution of total organic mass) and eBC-PM₁ (8 % of the
694 total eBC-PM₁) was associated with: a) low traffic emissions, b) household heating in winter, and c) the central heating for hot
695 water production for all the seasons which uses multiple fuel types in the Melpitz area. BBOA representing 7.9 % of the
696 contribution of total organic mass and 37 % of the total eBC-PM₁, showed a seasonal effect, emphasizing the impact of house
697 heating during winter. Similar to HOA, the presence of BBOA during summer was due to central heating which uses multiple
698 fuel types in the Melpitz area. The most dominant anthropogenic source was associated with CCOA with a 15.4 % contribution
699 of total organic mass and 55 % of the total eBC-PM₁ with the highest mass concentration and contribution of PM during winter
700 rather than summer. Although a certain fraction of CCOA could be linked to surrounding domestic heating (van Pinxteren et
701 al., 2020), it is rather associated with power plant emissions and long-range transport all year round which is supported by
702 cluster and back-trajectory analysis. LO-OOA and MO-OOA referred to oxidized oxygenated organic aerosol (32.4 % and
703 38.4 % of the contribution of total organic mass, respectively), were identified as a secondary organic aerosol with the highest
704 mass concentration during the cold months and the lowest mass concentration during the warm months. LO-OOA mass
705 concentration decreased during the day due to dilution, and the evaporation process resulted in aging into MO-OOA.

706 A combination of the NWR model and cluster analysis was used to better understand the origin of the aerosol reaching the
707 station. Overall, Melpitz is influenced by fifteen types of air masses, such as long-range continental, marine, and surrounding
708 emissions. During winter and summer time, easterly continental air masses, CS-A1 and WS-A1 with an anticyclonic pattern
709 come from Eastern Europe and showed a significant particle mass concentration, especially high POA (and CCOA) mass
710 concentration at the measurement site. Marine clusters, mostly coming from the south/west/north side with aged marine air
711 masses including nitrate and sulphate, also have important roles in the PM mass concentration at the Melpitz site over the
712 entire period (winter: CS-A2, CS-C2b, and CS-C2a, transition: TS-C, TS-A2 and TS-C2, and summer: WS-Ca, WS-C2, and

713 WS-A2). However, the surrounding emissions are recognized as another important source of emissions which include high
714 organic and inorganic components during winter and summer (CS-ST and WS-ST, respectively).

715

716 Our results emphasize the importance of the long-range transported emissions of coal combustion related aerosol particles
717 regardless of the season, which supports that the main CCOA source is related to coal power plants emissions. However, coal
718 power plants emissions not only affect the surrounding air quality but can also be transported over long distances. It is important
719 to note that the overall coal combustion mass concentration presented here can certainly be underestimated since the identified
720 CCOA factor is associated with freshly emitted organic aerosol and no factor associated with potential aged coal combustion
721 was identified. Because coal still is an important energy source in the European energy mix (68.4 % of all energy in the EU
722 was produced from coal, crude oil, and natural gas, Energy Statistics - an Overview - Statistics Explained, 2022) as well as on
723 a global scale and also that it still will be in use for the coming decades (until 2040, Europe's Coal Exit - Europe Beyond Coal :
724 Europe Beyond Coal, 2022), further researches should be done on the identification of coal emissions across Europe in order
725 to better understand its atmospheric aging processes.

726

727 **Acknowledgements**

728 This work is supported by the COST action CA16109 Chemical On-Line cOmpoSition and Source Apportionment of fine
729 aerosols (COLOSSAL), the SNF COST project SAMSAM IZCOZO_177063., by the infrastructure projects ACTRIS (EU
730 FP7, grant 262254), the RI-URBANS project under grant NO. 101036245, the ERA-PLANET, and transnational projects
731 SMURBS and iCUPE (grant agreement NO. 689443), and ACTRIS-2 (Grant 654109).

732 **References**

- 733 Aas, W., Tsyro, S., Bieber, E., Bergström, R., Ceburnis, D., Ellermann, T., Fagerli, H., Frölich, M., Gehrig, R.,
734 Makkonen, U., Nemitz, E., Otjes, R., Perez, N., Perrino, C., Prévôt, A. S. H., Putaud, J. P., Simpson, D., Spindler,
735 G., Vana, M., and Yttri, K. E.: Lessons learnt from the first EMEP intensive measurement periods, *Atmos. Chem.*
736 *Phys.*, 12(17), 8073–8094, <https://doi.org/10.5194/acp-12-8073-2012>, 2012.
- 737 Alfara, M. R., Prevot, A. S. H., Szidat, S., Sandradewi, J., Weimer, S., Lanz, V. A., Schreiber, D., Mohr, M., and
738 Baltensperger, U.: Identification of the mass spectral signature of organic aerosols from wood burning emissions,
739 *Environ. Sci. Technol.*, 41(16), 5770–5777, <https://doi.org/10.1021/es062289b>, 2007.
- 740 Allan, J. D., Delia, A. E., Coe, H., Bower, K. N., Alfara, M. R., Jimenez, J. L., Middlebrook, A. M., Drewnick, F.,
741 Onasch, T. B., Canagaratna, M. R., Jayne, J. T., and Worsnop, D. R.: A generalised method for the extraction of
742 chemically resolved mass spectra from Aerodyne aerosol mass spectrometer data, *J. Aerosol Sci.*, 35(7), 909–922,
743 <https://doi.org/10.1016/j.jaerosci.2004.02.007>, 2004.

744 Birmili, W., Heinke, K., Pitz, M., Matschullat, J., Wiedensohler, A., Cyrus, J., Wichmann, H. E., and Peters, A.: Particle
745 number size distributions in urban air before and after volatilisation, *Atmos. Chem. Phys.*, 10(10), 4643–4660,
746 <https://doi.org/10.5194/acp-10-4643-2010>, 2010.

747 Birmili, W., Schepanski, K., Ansmann, A., Spindler, G., Tegen, I., Wehner, B., Nowak, A., Reimer, E., Mattis, I., M
748 Uller, K., Brüggemann, E., Brüggemann, B., Gnauk, T., Herrmann, H., Wiedensohler, A., Althausen, D.,
749 Schladitz, A., Tuch, T., and Löschau, G.: A case of extreme particulate matter concentrations over Central Europe
750 caused by dust emitted over the southern Ukraine, *Atmos. Chem. Phys.*, 8, [www.atmos-chem-](http://www.atmos-chem-phys.net/8/997/2008/)
751 [phys.net/8/997/2008/](http://www.atmos-chem-phys.net/8/997/2008/), 2008.

752 Birmili, W., Stratmann, F., and Wiedensohler, A.: Technical note design of a DMA-based size spectrometer for a large
753 particle size range and stable operation, *J. Aerosol Sci.*, 30, Issue 4, 1999.

754 Birmili, W., Sun, J., Wiedensohler, A., Birmili, W., Sun, J., Weinhold, K., Merkel, M., Rasch, F., Spindler, G.,
755 Wiedensohler, A., Bastian, S., Löschau, G., Schladitz, A., Quass, U., Kuhlbusch, T. A. J., Kaminski, H., Cyrus,
756 J., Pitz, M., Gu, J., Peters, A., Flentje, H., Meinhardt, F., Schwerin, A., Bath, O., Ries, L., Gerwig, H., Wirtz, K.,
757 and Weber, S.: Enhanced Land Use Regression models for urban fine dust and ultrafine particle concentrations
758 View project Radon parallel measurements, View project Atmospheric aerosol measurements in the German
759 Ultrafine Aerosol Network (GUAN), <https://www.researchgate.net/publication/330910927>, 2015.

760 Birmili, W., Weinhold, K., Rasch, F., Sonntag, A., Sun, J., Merkel, M., Wiedensohler, A., Bastian, S., Schladitz, A.,
761 Löschau, G., Cyrus, J., Pitz, M., Gu, J., Kusch, T., Flentje, H., Quass, U., Kaminski, H., Kuhlbusch, T. A. J.,
762 Meinhardt, F., Schwerin, A., Bath, O., Ries, L., Gerwig, H., Wirtz, K., and Fiebig, M.: Long-term observations of
763 tropospheric particle number size distributions and equivalent black carbon mass concentrations in the German
764 Ultrafine Aerosol Network (GUAN), *Earth System Science Data*, 8(2), 355–382, [https://doi.org/10.5194/essd-8-](https://doi.org/10.5194/essd-8-355-2016)
765 [355-2016](https://doi.org/10.5194/essd-8-355-2016), 2016.

766 Birmili, W., Wiedensohler, A., Mueller, K., Birmili, W., Weinhold, K., Nordmann, S., Wiedensohler, A., Spindler, G.,
767 Müller, K., Herrmann, H., Gnauk, T., Pitz, M., Cyrus, J., Flentje, H., Nickel, C., J Kuhlbusch, T. A., Löschau, G.,
768 Haase, D., Meinhardt, F., F., Schwerin, A., Ries, L., and Wirtz, K.: Atmospheric aerosol measurements in the
769 German Ultrafine Aerosol Network (GUAN) Korngrößendifferenzierte Feinstaubbelastung in Straßennähe in
770 Ballungsgebieten Sachsens (2003-2005) View project Chemistry, Air Quality and Climate View project
771 Atmospheric aerosol measurements in the German Ultrafine Aerosol Network (GUAN) Part 1: Soot and particle
772 number size distributions, <https://www.researchgate.net/publication/232089057>, 2009.

773 Bootstrap Methods: Another Look at the Jackknife on JSTOR, [https://www.jstor.org/stable/2958830?origin=JSTOR-](https://www.jstor.org/stable/2958830?origin=JSTOR-pdf)
774 [pdf](https://www.jstor.org/stable/2958830?origin=JSTOR-pdf), 1979.

775 Bressi, M., Cavalli, F., Putaud, J. P., Fröhlich, R., Petit, J. E., Aas, W., Äijälä, M., Alastuey, A., Allan, J. D., Aurela,
776 M., Berico, M., Bougiatioti, A., Bukowiecki, N., Canonaco, F., Crenn, V., Dusanter, S., Ehn, M., Elsasser, M.,
777 Flentje, H., M., Flentje, H., Graf, P., Green, D. C., Heikkinen, L., Hermann, H., Holzinger, R., Hueglin, C.,

778 Keernik, H., Kiendler-Scharr, A., Kubelova, L., Lunder, C., Maasikmets, M., Makes, O., Malaguti, A.,
779 Mihalopoulos, N., Nicolas, J.B., O'Dowd, C., Ovadnevaite, J., Petralia, E., Poulain, L., Priestman, M., Riffault,
780 V., Ripoll, A., Schlag, P., Schwarz, J., Sciarec., J., Slowik, J., Sosedova, Y., Stavroulas, I., Teinmaa, E., Via, M.,
781 Vodickar, P., Williams, P.I., Wiedensohler, A., Young, D.E., Zhang, S., Favez, O., Minguillon, M.C., and Prevot,
782 A. S. H.: A European aerosol phenomenology - 7: High-time resolution chemical characteristics of submicron
783 particulate matter across Europe, *Atmos. Environ.*, X, 10, <https://doi.org/10.1016/j.aeaoa.2021.100108>, 2021.

784 Canagaratna, M. R., Jayne, J. T., Ghertner, D. A., Herndon, S., Shi, Q., Jimenez, J. L., Silva, P. J., Williams, P., Lanni,
785 T., Drewnick, F., Demerjian, K. L., Kolb, C. E., and Worsnop, D. R.: Chase studies of particulate emissions from
786 in-use New York City vehicles, *Aerosol Sci Technol.*, 38(6), 555–573,
787 <https://doi.org/10.1080/02786820490465504>, 2004.

788 Canagaratna, M. R., Jimenez, J. L., Kroll, J. H., Chen, Q., Kessler, S. H., Massoli, P., Hildebrandt Ruiz, L., Fortner, E.,
789 Williams, L. R., Wilson, K. R., Surratt, J. D., Donahue, N. M., Jayne, J. T., and Worsnop, D. R.: Elemental ratio
790 measurements of organic compounds using aerosol mass spectrometry: Characterization, improved calibration,
791 and implications, *Atmos. Chem. Phys.*, 15(1), 253–272, <https://doi.org/10.5194/acp-15-253-2015>, 2015.

792 Canonaco, F., Crippa, M., Slowik, J. G., Baltensperger, U., and Prévôt, A. S. H.: SoFi, an IGOR-based interface for the
793 efficient use of the generalized multilinear engine (ME-2) for the source apportionment: ME-2 application to
794 aerosol mass spectrometer data, *Atmos. Meas. Tech.*, 6(12), 3649–3661, [https://doi.org/10.5194/amt-6-3649-](https://doi.org/10.5194/amt-6-3649-2013)
795 [2013](https://doi.org/10.5194/amt-6-3649-2013), 2013.

796 Canonaco, F., Slowik, J. G., Baltensperger, U., and Prévôt, A. S. H.: Seasonal differences in oxygenated organic aerosol
797 composition: Implications for emissions sources and factor analysis, *Atmos. Chem. Phys.*, 15(12), 6993–7002,
798 <https://doi.org/10.5194/acp-15-6993-2015>, 2015.

799 Canonaco, F., Tobler, A., Chen, G., Sosedova, Y., Gates Slowik, J., Bozzetti, C., Rudolf Daellenbach, K., el Haddad,
800 I., Crippa, M., Huang, R. J., Furger, M., Baltensperger, U., and Prévôt, A. S. H.: A new method for long-term
801 source apportionment with time-dependent factor profiles and uncertainty assessment using SoFi Pro: Application
802 to 1 year of organic aerosol data. *Atmos. Meas. Tech.*, 14(2), 923–943, <https://doi.org/10.5194/amt-14-923-2021>,
803 2021.

804 Canonaco, F., Tobler, A., Chen, G., Sosedova, Y., Slowik, J. G., Bozzetti, C., Daellenbach, K. R., ElHaddad, I., Crippa,
805 M., Huang, R.-J., Furger, M., Baltensperger, U., and Prévôt, A. S. H.: A new method for long-term source
806 apportionment with time-dependent factor profiles and uncertainty assessment using SoFi Pro: application to one
807 year of organic aerosol data, *Atmos. Meas. Tech.*, 1–39, <https://doi.org/10.5194/amt-2020-204>, 2020.

808 Chazeau, B., el Haddad, I., Canonaco, F., Temime-Roussel, B., D'Anna, B., Gille, G., Mesbah, B., Prévôt, A. S. H.,
809 Wortham, H., and Marchand, N.: Organic aerosol source apportionment by using rolling positive matrix
810 factorization: Application to a Mediterranean coastal city, *Atmos. Environ.*, X, 14,
811 <https://doi.org/10.1016/j.aeaoa.2022.100176>, 2022.

812 Chen, G., Canonaco, F., Tobler, A., Aas, W., Alastuey, A., Allan, J., Atabakhsh, S., Aurela, M., Baltensperger, U.,
813 Bougiatioti, A., de Brito, J. F., Ceburnis, D., Chazeau, B., Chebaicheb, H., Daellenbach, K. R., Ehn, M., el Haddad,
814 I., Eleftheriadis, K., Favez, O., Flentje, H., Font, A., Fossum, K., Freney, E., Gini, M., Green, D.C., Heikkinen,
815 L., Herrmann, H., Kalogridis, A., Keernik, H., Lhotka, R., Lin, C., Lunder, C., Maasikmets, M., Manousakas,
816 M.I., Marchand, N., Marin, C., Marmureanu, L., Mihalopoulos, N., Mocnika, G., Nęckia, J., O'Dowd, C.,
817 Ovadnevaite, J., Petera, T., Petita, J.E., Pikridasa, M., Matthew Platt, S., Pokorna, P., Poulain, L., Priestman, M.,
818 Riffault, V., Rinaldia, M., Rozanskia, K., Schwarz, J., Sciarea, J., Simon, L., Skiba, A., Slowik, J.G., Sosedova,
819 Y., Stavroulas, I., Styszkoa, K., Teinmaa, E., Timonen, H., Tremper, A., Vasilescu, J., Via, M., Vodicka, P.,
820 Wiedensohler, A., Zografou, O., Cruz Minguillon, M., and Prévôt, A. S. H.: European aerosol phenomenology –
821 8: Harmonised source apportionment of organic aerosol using 22 Year-long ACSM/AMS datasets, *Environ. Int.*,
822 166, <https://doi.org/10.1016/j.envint.2022.107325>, 2022.

823 Chen, G., Sosedova, Y., Canonaco, F., Fröhlich, R., Tobler, A., Vlachou, A., Daellenbach, K., Bozzetti, C., Hueglin,
824 C., Graf, P., Baltensperger, U., Slowik, J., el Haddad, I., and Prévôt, A.: Time dependent source apportionment of
825 submicron organic aerosol for a rural site in an alpine valley using a rolling PMF window, *Atmos. Chem. Phys.*,
826 1–52, <https://doi.org/10.5194/acp-2020-1263>, 2020.

827 Chen, G., Sosedova, Y., Canonaco, F., Fröhlich, R., Tobler, A., Vlachou, A., Daellenbach, K. R., Bozzetti, C., Hueglin,
828 C., Graf, P., Baltensperger, U., Slowik, J. G., el Haddad, I., and Prévôt, A. S. H.: Time-dependent source
829 apportionment of submicron organic aerosol for a rural site in an alpine valley using a rolling positive matrix
830 factorisation (PMF) window, *Atmos. Chem. Phys.*, 21(19), 15081–15101, [https://doi.org/10.5194/acp-21-15081-](https://doi.org/10.5194/acp-21-15081-2021)
831 [2021](https://doi.org/10.5194/acp-21-15081-2021), 2021.

832 Crippa, M., Canonaco, F., Lanz, V. A., Äijälä, M., Allan, J. D., Carbone, S., Capes, G., Ceburnis, D., Dall'Osto, M.,
833 Day, D. A., DeCarlo, P. F., Ehn, M., Eriksson, A., Freney, E., Ruiz, L. H., Hillamo, R., Jimenez, J. L., Junninen,
834 H., Kiendler-Scharr, A., Kortelainen, A.-M., Kulmala, M., Laaksonen, A., Mensah10, A.A., Mohr1, C., Nemitz,
835 E., O'Dowd, C., Ovadnevaite, J., Pandis, S. N., Petäjä, T., Poulain, L., Saarikoski, S., Sellegri, K., Swietlicki, E.,
836 Tiitta, P., Worsnop, D. R., Baltensperger, U., and Prévôt, A. S. H.: Organic aerosol components derived from 25
837 AMS data sets across Europe using a consistent ME-2 based source apportionment approach. *Atmos. Chem. Phys.*,
838 14(12), 6159–6176, <https://doi.org/10.5194/acp-14-6159-2014>, 2014.

839 Crippa, M., Decarlo, P. F., Slowik, J. G., Mohr, C., Heringa, M. F., Chirico, R., Poulain, L., Freutel, F., Sciare, J., Cozic,
840 J., di Marco, C. F., Elsassner, M., Nicolas, J. B., Marchand, N., Abidi, E., Wiedensohler, A., Drewnick, F.,
841 Schneider, J., Borrmann, S., Nemitz, E., Zimmermann, R., Jaffrezo, J.-L., Prevot, A. S. H., and Baltensperger, U.
842 Wintertime aerosol chemical composition and source apportionment of the organic fraction in the metropolitan
843 area of Paris, *Atmos. Chem. Phys.*, 13(2), 961–981, <https://doi.org/10.5194/acp-13-961-2013>, 2013.

844 Daellenbach, K. R., Uzu, G., Jiang, J., Cassagnes, L. E., Leni, Z., Vlachou, A., Stefanelli, G., Canonaco, F., Weber, S.,
845 Segers, A., Kuenen, J. J. P., Schaap, M., Favez, O., Albinet, A., Aksoyoglu, S., Dommen, J., Baltensperger, U.,

846 Geiser, M., el Haddad, I., Jaffrezo, J.L., and Prévôt, A. S. H.: Sources of particulate-matter air pollution and its
847 oxidative potential in Europe, *Nature*, 587(7834), 414–419, <https://doi.org/10.1038/s41586-020-2902-8>, 2020.

848 Dall’Osto, M., Ovadnevaite, J., Ceburnis, D., Martin, D., Healy, R. M., O’Connor, I. P., Kourchev, I., Sodeau, J. R.,
849 Wenger, J. C., and O’Dowd, C.: Characterization of urban aerosol in Cork city (Ireland) using aerosol mass
850 spectrometry. *Atmos. Chem. Phys.*, 13(9), 4997–5015, <https://doi.org/10.5194/acp-13-4997-2013>, 2013.

851 Draxler, R.R. and Hess, G.D.: Description of the HYSPLIT-4 Modeling System, NOAA Technical Memorandum ERL
852 ARL-224, NOAA Air Resources Laboratory, Silver Spring, 1-24, 1997.

853 Dudoitis, V., Byčenkienė, S., Plauškaite, K., Bozzetti, C., Fröhlich, R., Mordas, G., and Ulevičius, V.: Spatial
854 distribution of carbonaceous aerosol in the southeastern Baltic Sea region (event of grass fires), *Acta Geophysica*,
855 64(3), 711–731, <https://doi.org/10.1515/acgeo-2016-0018>, 2016.

856 Energy statistics - an overview - Statistics Explained, [https://ec.europa.eu/eurostat/statistics-
857 explained/index.php?title=Energy_statistics_-_an_overview](https://ec.europa.eu/eurostat/statistics-explained/index.php?title=Energy_statistics_-_an_overview), 2022.

858 Europe’s coal exit - Europe Beyond Coal: Europe Beyond Coal, <https://beyond-coal.eu/europes-coal-exit/>, 2022.

859 Fröhlich, R., Crenn, V., Setyan, A., Belis, C. A., Canonaco, F., Favez, O., Riffault, V., Slowik, J. G., Aas, W., Aijälä,
860 M., Alastuey, A., Artiñano, B., Bonnaire, N., Bozzetti, C., Bressi, M., Carbone, C., Coz, E., Croteau, P. L.,
861 Cubison, M. J., Esser-Gietl, J. K., Green, D. C., Gros, V., Heikkinen, L., Herrmann, H., Jayne, J. T., Lunder, C.
862 R., Minguillón, M. C., Mocnik, G., O’Dowd, C. D., Ovadnevaite, J., Petralia, E., Poulain, L., Priestman, M., Ripol,
863 Sarda-Estève, A., R., Wiedensohler, A., Baltensperger, U., Sciare, J., and Prévôt, A. S. H., ACTRIS ACSM
864 intercomparison - Part 2: Intercomparison of ME-2 organic source apportionment results from 15 individual, co-
865 located aerosol mass spectrometers, *Atmos. Meas. Tech.*, 8(6), 2555–2576, [https://doi.org/10.5194/amt-8-2555-
866 2015](https://doi.org/10.5194/amt-8-2555-2015), 2015.

867 Fröhlich, R., Cubison, M. J., Slowik, J. G., Bukowiecki, N., Prévôt, A. S. H., Baltensperger, U., Schneider, J., Kimmel,
868 J. R., Gonin, M., Rohner, U., Worsnop, D. R., and Jayne, J. T.: The ToF-ACSM: A portable aerosol chemical
869 speciation monitor with TOFMS detection. *Atmos. Meas. Tech.*, 6(11), 3225–3241, [https://doi.org/10.5194/amt-
870 6-3225-2013](https://doi.org/10.5194/amt-6-3225-2013), 2013.

871 Gilardoni, S., Massoli, P., Paglione, M., Giulianelli, L., Carbone, C., Rinaldi, M., Decesari, S., Sandrini, S., Costabile,
872 F., Gobbi, G. P., Pietrogrande, M. C., Visentin, M., Scotto, F., Fuzzi, S., and Facchini, M. C.: Direct observation
873 of aqueous secondary organic aerosol from biomass-burning emissions, *Proceedings of the National Academy of
874 Sciences of the United States of America*, 113(36), 10013–10018, <https://doi.org/10.1073/pnas.1602212113>,
875 2016.

876 Heikkinen, L., Äijälä, M., Daellenbach, K., Chen, G., Garmash, O., Aliaga, D., Graeffe, F., Rätty, M., Luoma, K., Aalto,
877 P., Kulmala, M., Petäjä, T., Worsnop, D., and Ehn, M.: Eight years of sub-micrometre organic aerosol composition
878 data from the boreal forest characterized using a machine-learning approach, *Atmos. Chem. Phys.*, 1–47,
879 <https://doi.org/10.5194/acp-2020-868>, 2020.

880 Henry, R., Norris, G. A., Vedantham, R., and Turner, J. R.: Source region identification using kernel smoothing,
881 Environ. Sci. Technol., 43(11), 4090–4097, <https://doi.org/10.1021/es8011723>, 2009.

882 Huang, S., Wu, Z., Poulain, L., van Pinxteren, M., Merkel, M., Assmann, D., Herrmann, H., and Wiedensohler, A.:
883 Source apportionment of the organic aerosol over the Atlantic Ocean from 53°N to 53°S: Significant contributions
884 from marine emissions and long-range transport, Atmos. Chem. Phys., 18(24), 18043–18062,
885 <https://doi.org/10.5194/acp-18-18043-2018>, 2018.

886 Huang, W., Saathoff, H., Shen, X., Ramisetty, R., Leisner, T., and Mohr, C.: Seasonal characteristics of organic aerosol
887 chemical composition and volatility in Stuttgart, Germany, Atmos. Chem. Phys., 19(18), 11687–11700,
888 <https://doi.org/10.5194/acp-19-11687-2019>, 2019.

889 Hussein, T., Karppinen, A., Kukkonen, J., Härkönen, J., Aalto, P. P., Hämeri, K., Kerminen, V. M., and Kulmala, M.:
890 Meteorological dependence of size-fractionated number concentrations of urban aerosol particles, Atmos.
891 Environ., 40(8), 1427–1440, <https://doi.org/10.1016/j.atmosenv.2005.10.061>, 2006.

892 Iapalucci, T. L., Demski, R. J., and Bienstock, D.: Chlorine in Coal Combustion. United States Department of the
893 Interior, Bureau of Mines Report of Investigation 7260s, 1969.

894 Iinuma, Y., Engling, G., Puxbaum, H., and Herrmann, H.: A highly resolved anion-exchange chromatographic method
895 for determination of saccharidic tracers for biomass combustion and primary bio-particles in atmospheric aerosol,
896 Atmos. Environ., 43(6), 1367–1371, <https://doi.org/10.1016/j.atmosenv.2008.11.020>, 2009.

897 Jayne, J. T., Leard, D. C., Zhang, X., Davidovits, P., Smith, K. A., Kolb, C. E., and Worsnop, D. R.: Development of
898 an Aerosol Mass Spectrometer for Size and Composition Analysis of Submicron Particles, Aerosol Sci Technol.,
899 33:1-2, 48-70, <https://doi.org/10.1080/027868200410840>, 2000.

900 Jimenez, J. L., Canagaratna, M. R., Donahue, N. M., Prevot, A. S. H., Zhang, Q., Kroll, J. H., DeCarlo, P. F., Allan, J.
901 D., Coe, H., Ng, N. L., Aiken, A. C., Docherty, K. S., Ulbrich, I. M., Grieshop, A. P., Robinson, A. L., Duplissy,
902 J., Smith, J. D., Wilson, K. R., Lanz, V. A., Hueglin, C., Sun, Y. L., Tian, J., Laaksonen, A., Raatikainen, T.,
903 Rautiainen, J., Vaattovaara, P., Ehn, M., Kulmala, M., Tomlinson, J. M., Collins, D. R., Cubison, M. J., Dunlea,
904 E. J., Huffman, J. A., Onasch, T. B., Alfarra, M. R., Williams, P. I., Bower, K., Kondo, Y., Schneider, J.,
905 Drewnick, F., Borrmann, S., Weimer, S., Demerjian, K., Salcedo, D., Cottrell, L., Griffin, R., Takami, A., Miyoshi,
906 T., Hatakeyama, S., Shimojo, A., Sun, J. Y., Zhang, Y. M., Dzepina, K., Kimmel, J. R., Sueper, D., Jayne, J. T.,
907 Herndon, S. C., Trimborn, A. M., Williams, L. R., Wood, E. C., Middlebrook, A. M., Kolb, C. E., Baltensperger,
908 U., and Worsnop, D. R.: Evolution of organic aerosols in the atmosphere. Science, 326(5959), 1525–1529,
909 <https://doi.org/10.1126/science.1180353>, 2009.

910 Katsanos, D., Bougiatioti, A., Liakakou, E., Kaskaoutis, D. G., Stavroulas, I., Paraskevopoulou, D., Lianou, M.,
911 Psiloglou, B. E., Gerasopoulos, E., Pilinis, C., and Mihalopoulos, N.: Optical properties of near-surface urban
912 aerosols and their chemical tracing in a mediterranean city (Athens), Aerosol and Air Quality Research, 19(1),
913 49–70, <https://doi.org/10.4209/aaqr.2017.11.0544>, 2019.

914 Keck, L. and Wittmaack, K.: Effect of filter type and temperature on volatilisation losses from ammonium salts in
915 aerosol matter, *Atmos. Environ.*, 39, 4093–4100, <https://doi.org/10.1016/j.atmosenv.2005.03.029>, 2005.

916 Kiendler-Scharr, A., Mensah, A. A., Friese, E., Topping, D., Nemitz, E., Prevot, A. S. H., Äijälä, M., Allan, J., Canonaco,
917 F., Canagaratna, M., Carbone, S., Crippa, M., Dall'Osto, M., Day, D. A., de Carlo, P., di Marco, C. F., Elbern, H.,
918 Eriksson, A., Freney, E., Hao, L., Herrmann, H., Hildebrandt, L., Hillamo, R., Jimenez, J. L., Laaksonen, A.,
919 McFiggans, G., Mohr, C., O'Dowd, C., Otjes, R., Ovadnevaite, J., Pandis, S. N., Poulain, L., Schlag, P., Sellegri,
920 K., Swietlicki, E., Tiitta, P., Vermeulen, A., Wahner, A., Worsnop, D. and Wu, H. C.: Ubiquity of organic nitrates
921 from night time chemistry in the European submicron aerosol, *Geophysical Research Letters*, 43(14), 7735–7744,
922 <https://doi.org/10.1002/2016GL069239>, 2016.

923 Kodros, J., Papanastasiou, D., Paglionea, M., Masiol, M., Squizzato, S., Florou, K., Skyllakou, K., Kaltsonoudis, C.,
924 Nenesa, A., and Pandisa, S.: Rapid dark aging of biomass burning as an overlooked source of oxidized organic
925 aerosol, *PNAS*, <https://doi.org/10.1073/pnas.1602212113>, 2020.

926 Kumar, V., Giannoukos, S., Haslett, S. L., Tong, Y., Singh, A., Bertrand, A., Lee, C. P., Wang, D. S., Bhattu, D.,
927 Stefanelli, G., Dave, J. S., Puthussery, J. v., Qi, L., Vats, P., Rai, P., Casotto, R., Satish, R., Mishra, S., Pospisilova,
928 V., C., Bell, D.M., Ganguly, D., Verma, V., Rastogi, N., Baltensperger, U., Tripathi, S.N., Prévôt, A.S.H., and
929 Slowik, J. G.: Highly time-resolved chemical speciation and source apportionment of organic aerosol components
930 in Delhi, India, using extractive electrospray ionization mass spectrometry, *Atmos. Chem. Phys.*, 22(11), 7739–
931 7761, <https://doi.org/10.5194/acp-22-7739-2022>, 2022.

932 Laborde, M., Crippa, M., Tritscher, T., Jurányi, Z., Decarlo, P. F., Temime-Roussel, B., Marchand, N., Eckhardt, S.,
933 Stohl, A., Baltensperger, U., Prévôt, A. S. H., Weingartner, E., and Gysel, M.: Black carbon physical properties
934 and mixing state in the European megacity Paris, *Atmos. Chem. Phys.*, 13(11), 5831–5856,
935 <https://doi.org/10.5194/acp-13-5831-2013>, 2013.

936 Lanz, V., Prevot, A., Alfarra, M., Weimer, S., Mohr, C., DeCarlo, P., Gianini, M., Hueglin, C., Schneider, J., Favez, O.,
937 D'Anna, B., George, C., and Baltensperger, U.: Characterization of aerosol chemical composition with aerosol
938 mass spectrometry in Central Europe: an overview, *Atmos. Chem. Phys.*, 10, 10453–10471, 2010.

939 Li, G., Lei, W., Bei, N., and Molina, L. T.: Contribution of garbage burning to chloride and PM 2.5 in Mexico City,
940 *Atmos. Chem. Phys.*, 12(18), 8751–8761, <https://doi.org/10.5194/acp-12-8751-2012>, 2012.

941 Lin, C., Ceburnis, D., Hellebust, S., Buckley, P., Wenger, J., Canonaco, F., Prévôt, A. S. H., Huang, R. J., O'Dowd, C.,
942 and Ovadnevaite, J.: Characterization of Primary Organic Aerosol from Domestic Wood, Peat, and Coal Burning
943 in Ireland, *Environ. Sci. Technol.*, 51(18), 10624–10632, <https://doi.org/10.1021/acs.est.7b01926>, 2017.

944 Liu, P. S. K., Deng, R., Smith, K. A., Williams, L. R., Jayne, J. T., Canagaratna, M. R., Moore, K., Onasch, T. B.,
945 Worsnop, D. R., and Deshler, T.: Transmission efficiency of an aerodynamic focusing lens system: Comparison
946 of model calculations and laboratory measurements for the aerodyne aerosol mass spectrometer, *Aerosol Sci
947 Technol.*, 41(8), 721–733, <https://doi.org/10.1080/02786820701422278>, 2007.

948 Ma, N., Birmili, W., Müller, T., Tuch, T., Cheng, Y. F., Xu, W. Y., Zhao, C. S., and Wiedensohler, A.: Tropospheric
949 aerosol scattering and absorption over central Europe: A closure study for the dry particle state. *Atmos. Chem.*
950 *Phys.*, 14(12), 6241–6259, <https://doi.org/10.5194/acp-14-6241-2014>, 2014.

951 Marin, C., Marmureanu, L., Rado, C., Dodosci, A., Stan, C., Toanca, F., Preda, L., and Antonescu, B.: Wintertime
952 Variations of Gaseous Atmospheric Constituents in Bucharest Peri-Urban Area, *Atmosphere*, 10(8), 478;
953 <https://doi.org/10.3390/atmos10080478>, 2019.

954 Middlebrook, A. M., Bahreini, R., Jimenez, J. L., and Canagaratna, M. R.: Evaluation of composition-dependent
955 collection efficiencies for the Aerodyne aerosol mass spectrometer using field data. *Aerosol Sci Technol.*, 46(3),
956 258–271, <https://doi.org/10.1080/02786826.2011.620041>, 2012.

957 Ng, N. L., Canagaratna, M. R., Zhang, Q., Jimenez, J. L., Tian, J., Ulbrich, I. M., Kroll, J. H., Docherty, K. S., Chhabra,
958 P. S., Bahreini, R., Murphy, S. M., Seinfeld, J. H., Hildebrandt, L., Donahue, N. M., Decarlo, P. F., Lanz, V. A.,
959 Prévôt, A. S. H., Dinar, E., Rudich, Y., and Worsnop, D. R.: Organic aerosol components observed in Northern
960 Hemispheric datasets from Aerosol Mass Spectrometry, *Atmos. Chem. Phys.*, 10(10), 4625–4641,
961 <https://doi.org/10.5194/acp-10-4625-2010>, 2010.

962 Ng, N. L., Herndon, S. C., Trimborn, A., Canagaratna, M. R., Croteau, P. L., Onasch, T. B., Sueper, D., Worsnop, D.
963 R., Zhang, Q., Sun, Y. L., and Jayne, J. T.: An Aerosol Chemical Speciation Monitor (ACSM) for routine
964 monitoring of the composition and mass concentrations of ambient aerosol, *Aerosol Sci Technol.*, 45(7), 780–
965 794, <https://doi.org/10.1080/02786826.2011.560211>, 2011.

966 O’Dowd, C., Ceburnis, D., Ovadnevaite, J., Vaishya, A., Rinaldi, M., and Facchini, M. C.: Do anthropogenic,
967 continental or coastal aerosol sources impact on a marine aerosol signature at Mace Head? *Atmos. Chem. Phys.*,
968 14(19), 10687–10704, <https://doi.org/10.5194/acp-14-10687-2014>, 2014.

969 Ovadnevaite, J., Ceburnis, D., Leinert, S., Dall’Osto, M., Canagaratna, M., O’Doherty, S., Berresheim, H., and O’Dowd,
970 C.: Submicron NE Atlantic marine aerosol chemical composition and abundance: Seasonal trends and air mass
971 categorization, *J. Geophys. Res.*, 119(20), 11,850–11,863, <https://doi.org/10.1002/2013JD021330>, 2014.

972 Paatero, P.: Least squares formulation of robust non-negative factor analysis, In *Chemometrics and Intelligent*
973 *Laboratory Systems*, 37, 1997.

974 Paatero, P.: The Multilinear Engine- A Table-Driven, Least Squares Program for Solving Multilinear Problems,
975 Including the n-Way Parallel Factor Analysis Model, *J Comput Graph Stat.*, 8(4), 854–888,
976 <https://doi.org/10.1080/10618600.1999.10474853>, 1999.

977 Paatero, P., and Tappert, U.: Positive matrix factorization: A non-negative factor model with optimal utilization of error
978 estimates of data values *, *ENVIRONMETRICS*, 5, 111–126, 1994.

979 Paglione, M., Gilardoni, S., Rinaldi, M., Decesari, S., Zanca, N., Sandrini, S., Giulianelli, L., Bacco, D., Ferrari, S.,
980 Poluzzi, V., Scotto, F., Trentini, A., Poulain, L., Herrmann, H., Wiedensohler, A., Canonaco, F., Prévôt, A. S. H.,
981 Massoli, P., Carbone, C., Bell, D.M., Ganguly, D., Verma, V., Rastogi, N., Baltensperger, U., Tripathi, S.N.,

982 Prévôt, A.S.H., and Fuzzi, S.: The impact of biomass burning and aqueous-phase processing on air quality: A
983 multi-year source apportionment study in the Po Valley, Italy, *Atmos. Chem. Phys.*, 20(3), 1233–1254,
984 <https://doi.org/10.5194/acp-20-1233-2020>, 2020.

985 Parworth, C., Fast, J., Mei, F., Shippert, T., Sivaraman, C., Tilp, A., Watson, T., and Zhang, Q.: Long-term
986 measurements of submicrometer aerosol chemistry at the Southern Great Plains (SGP) using an Aerosol Chemical
987 Speciation Monitor (ACSM), *Atmos. Environ.*, 106, 43–55, <https://doi.org/10.1016/j.atmosenv.2015.01.060>,
988 2015.

989 Petit, J.-E., Favez, O., Sciare, J., Crenn, V., Sarda-Esteve, R., Bonnaire, N., Mocnik, G., Dupont, J. C., Haeffelin, M.,
990 Leoz-Garziandia, E., Sarda, R., Petit, J.-E., Favez, O., Sciare, J., Crenn, V., Sarda-Estève, R., Bonnaire, N.,
991 Močnik, G., Dupont, J.-C., Haeffelin, M., and Leoz-Garziandia, E.: Two years of near real-time chemical
992 composition of submicron aerosols in the region of Paris using an Aerosol Chemical Speciation Monitor (ACSM)
993 and a multi-wavelength Aethalometer, *European Geosciences Union*, 15(6), 2985–3005,
994 <https://doi.org/10.5194/acpd-14-24221-2014j>, 2015.

995 Petzold, A., and Schönlinner, M.: Multi-angle absorption photometry - A new method for the measurement of aerosol
996 light absorption and atmospheric black carbon, *J. Aerosol Sci.*, 35(4), 421–441,
997 <https://doi.org/10.1016/j.jaerosci.2003.09.005>, 2004.

998 Pope, C. A., and Dockery, D. W., Health Effects of Fine Particulate Air Pollution: Lines that Connect, *J. Air & Waste*
999 *Manage. Assoc* 56, 35, <https://doi.org/10.1080/10473289.2006.10464485> 2006.

1000 Poulain, L., Birmili, W., Canonaco, F., Crippa, M., Wu, Z. J., Nordmann, S., Spindler, G., Prévôt, A. S. H.,
1001 Wiedensohler, A., and Herrmann, H.: Chemical mass balance of 300 °c non-volatile particles at the tropospheric
1002 research site Melpitz, Germany, *Atmos. Chem. Phys.*, 14(18), 10145–10162, [https://doi.org/10.5194/acp-14-](https://doi.org/10.5194/acp-14-10145-2014)
1003 [10145-2014](https://doi.org/10.5194/acp-14-10145-2014), 2014.

1004 Poulain, L., Fahlbusch, B., Spindler, G., Müller, K., van Pinxteren, D., Wu, Z., Iinuma, Y., Birmili, W., Wiedensohler,
1005 A., and Herrmann, H.: Source apportionment and impact of long-range transport on carbonaceous aerosol particles
1006 in central Germany during HCCT-2010, *Atmos. Chem. Phys.*, 21(5), 3667–3684, [https://doi.org/10.5194/acp-21-](https://doi.org/10.5194/acp-21-3667-2021)
1007 [3667-2021](https://doi.org/10.5194/acp-21-3667-2021), 2021.

1008 Poulain, L., Spindler, G., Birmili, W., Plass-Dülmer, C., Wiedensohler, A., and Herrmann, H.: Seasonal and diurnal
1009 variations of particulate nitrate and organic matter at the IfT research station Melpitz. *Atmos. Chem. Phys.*, 11(24),
1010 12579–12599, <https://doi.org/10.5194/acp-11-12579-2011>, 2011.

1011 Poulain, L., Spindler, G., Grüner, A., Tuch, T., Stieger, B., Pinxteren, D. van, Petit, J. E., Favez, O., Herrmann, H., and
1012 Wiedensohler, A.: Multi-year ACSM measurements at the central European research station Melpitz (Germany)-
1013 Part 1: Instrument robustness, quality assurance, and impact of upper size cutoff diameter, *Atmos. Meas. Tech.*,
1014 13(9), 4973–4994, <https://doi.org/10.5194/amt-13-4973-2020>, 2020.

1015 Qi, L., Vogel, A. L., Esmailirad, S., Cao, L., Zheng, J., Jaffrezo, J. L., Fermo, P., Kasper-Giebl, A., Daellenbach, K.
1016 R., Chen, M., Ge, X., Baltensperger, U., Prévôt, A. S. H., and Slowik, J. G.: A 1-year characterization of organic
1017 aerosol composition and sources using an extractive electrospray ionization time-of-flight mass spectrometer
1018 (EESI-TOF), *Atmos. Chem. Phys.*, 20(13), 7875–7893, <https://doi.org/10.5194/acp-20-7875-2020>, 2020.

1019 Saha, P., Kylystov, A., and Grieshop, A.: Downwind evolution of the volatility and mixing state of near-road aerosols
1020 near a US interstate highway, *ACP*, <https://doi.org/10.5194/acp-18-2139>, 2018.

1021 Schaap, M., Spindler, G., Schulz, M., Acker, K., Maenhaut, W., Berner, A., Wieprecht, W., Streit, N., Muller, K.,
1022 Bruggemann, E., Chi, X., Putaud, J. P., Hittenberger, R., Puxbaum, H., Baltensperger, U., and ten Brink, H.:
1023 Artefacts in the sampling of nitrate studied in the “INTERCOMP” campaigns of EUROTRAC-AEROSOL,
1024 *Atmos. Environ.*, 38, 6487–6496, <https://doi.org/10.1016/j.atmosenv.2004.08.026>, 2004.

1025 Schlag, P., Kiendler-Scharr, A., Johannes Blom, M., Canonaco, F., Sebastiaan Henzing, J., Moerman, M., Prévôt, A. S.
1026 H., and Holzinger, R.: Aerosol source apportionment from 1-year measurements at the CESAR tower in Cabauw,
1027 the Netherlands, *Atmos. Chem. Phys.*, 16(14), 8831–8847, <https://doi.org/10.5194/acp-16-8831-2016>, 2016.

1028 Schmale, J., Henning, S., Henzing, B., Keskinen, H., Sellegri, K., Ovadnevaite, J., Bougiatioti, A., Kalivitis, N.,
1029 Stavroulas, I., Jefferson, A., Park, M., Schlag, P., Kristensson, A., Iwamoto, Y., Pringle, K., Reddington, C., Aalto,
1030 P., Äijälä, M., Baltensperger, U., Bialek, J., Birmili, W., Bukowiecki, N., Ehn, M., Fjæraa, A., Fiebig, M., Frank,
1031 G., Fröhlich, R., Frumau, A., Furuya, M., Hammer, E., Heikkinen, L., Herrmann, E., Holzinger, R., Hyono, H.,
1032 Kanakidou, M., Kiendler-Scharr, A., Kinouchi, K., Kos, G., Kulmala, M., Mihalopoulos, N., Motos, G., Nenes,
1033 A., O’Dowd, C., Paramonov, M., Petäjä, T., Picard, D., Poulain, L., Prévôt, A., Slowik, J., Sonntag, A., Swietlicki,
1034 E., Svenningsson, B., Tsurumaru, H., Wiedensohler, A., Wittbom, C., Ogren, J., Matsuki, A., Yum, S., Myhre,
1035 G., Carslaw, K., Stratmann F., and Gysel, M.: Collocated observations of cloud condensation nuclei, particle size
1036 distributions, and chemical composition. *Sci Data* 4, 170003, <https://doi.org/10.1038/sdata.2017.3>, 2017.

1037 Seinfeld, J. H., and Pandis, S. N.: *Atmospheric Chemistry and Physics: From Air Pollution to Climate Change*, 3rd
1038 Edition, 1152, ISBN 9781118947401, 2006.

1039 Shi, Y., Chen, J., Hu, D., Wang, L., Yang, X., and Wang, X.: Airborne submicron particulate (PM₁) pollution in
1040 Shanghai, China: Chemical variability, formation/dissociation of associated semi-volatile components and the
1041 impacts on visibility, *Science of the Total Environment*, 473–474, 199–206,
1042 <https://doi.org/10.1016/j.scitotenv.2013.12.024>, 2014.

1043 Shrivastava, M., Cappa, C. D., Fan, J., Goldstein, A. H., Guenther, A. B., Jimenez, J. L., Kuang, C., Laskin, A., Martin,
1044 S. T., Ng, N. L., Petaja, T., Pierce, J. R., Rasch, P. J., Roldin, P., Seinfeld, J. H., Shilling, J., Smith, J. N., Thornton,
1045 J. A., Volkamer, R., Wang, J., Worsnop, D.R., Zaveri, R.A., Zelenyuk, A., and Zhang, Q.: Recent advances in
1046 understanding secondary organic aerosol: Implications for global climate forcing, *Reviews of Geophysics*, 55(2),
1047 509–559, <https://doi.org/10.1002/2016RG000540>, 2017.

1048 Simoneit, B. R. T., and Elias, V. O.: Detecting Organic Tracers from Biomass Burning in the Atmosphere, *Marine*
1049 *Pollution Bulletin*, 42, 10, 805-810, DOI: [10.1016/s0025-326x\(01\)00094-7](https://doi.org/10.1016/s0025-326x(01)00094-7), 2001.

1050 Simoneit, B. R. T., Schauer, J. J., Nolte, C. G., Oros, D. R., Elias, V. O., Fraser, M. P., Rogge, W. F., and Cass, G. R.:
1051 Levoglucosan, a tracer for cellulose in biomass burning and atmospheric particles, *Atmos. Environ.*, 33, 173-182,
1052 [https://doi.org/10.1016/S1352-2310\(98\)00145-9](https://doi.org/10.1016/S1352-2310(98)00145-9), 1999.

1053 Spindler, G., Brüggemann, E., Gnauk, T., Grüner, A., Müller, K., and Herrmann, H.: A four-year size-segregated
1054 characterization study of particles PM₁₀, PM_{2.5} and PM₁ depending on air mass origin at Melpitz, *Atmos.*
1055 *Environ.*, 44(2), 164–173, <https://doi.org/10.1016/j.atmosenv.2009.10.015>, 2010.

1056 Spindler, G., Gnauk, T., Grüner, A., Iinuma, Y., Müller, K., Scheinhardt, S., and Herrmann, H.: Size-segregated
1057 characterization of PM₁₀ at the EMEP site Melpitz (Germany) using a five-stage impactor: A six-year study, *J.*
1058 *Atmos. Chem.*, 69(2), 127–157, <https://doi.org/10.1007/s10874-012-9233-6>, 2012.

1059 Spindler, G., Grüner, A., Müller, K., Schlimper, S., and Herrmann, H.: Long-term size-segregated particle (PM₁₀,
1060 PM_{2.5}, PM₁) characterization study at Melpitz - Influence of air mass inflow, weather conditions and season, *J.*
1061 *Atmos. Chem.*, 70(2), 165–195, <https://doi.org/10.1007/s10874-013-9263-8>, 2013.

1062 Spindler, G., Müller, K., Brüggemann, E., Gnauk, T., and Herrmann, H.: Long-term size-segregated characterization of
1063 PM₁₀, PM_{2.5}, and PM₁ at the IfT research station Melpitz downwind of Leipzig (Germany) using high and low-
1064 volume filter samplers, *Atmos. Environ.*, 38(31), 5333–5347, <https://doi.org/10.1016/j.atmosenv.2003.12.047>,
1065 2004.

1066 Stavroulas, I., Bougiatioti, A., Grivas, G., Paraskevopoulou, D., Tsagkaraki, M., Zarmpas, P., Liakakou, E.,
1067 Gerasopoulos, E., and Mihalopoulos, N.K: Sources and processes that control the submicron organic aerosol
1068 composition in an urban Mediterranean environment (Athens): A high temporal-resolution chemical composition
1069 measurement study, *Atmos. Chem. Phys.*, 19(2), 901–919, <https://doi.org/10.5194/acp-19-901-2019>, 2019.

1070 Stieger, B., Spindler, G., Fahlbusch, B., Müller, K., Grüner, A., Poulain, L., Thöni, L., Seitzler, E., Wallasch, M., and
1071 Herrmann, H.: Measurements of PM₁₀ ions and trace gases with the online system MARGA at the research station
1072 Melpitz in Germany – A five-year study, *J. Atmos. Chem.*, 75(1), 33–70, [https://doi.org/10.1007/s10874-017-](https://doi.org/10.1007/s10874-017-9361-0)
1073 [9361-0](https://doi.org/10.1007/s10874-017-9361-0), 2018.

1074 Sun, J., Birmili, W., Hermann, M., Tuch, T., Weinhold, K., Merkel, M., Rasch, F., Müller, T., Schladitz, A., Bastian,
1075 S., Löschau, G., Cyrus, J., Gu, J., Flentje, H., Briel, B., Asbach, C., Kaminski, H., Ries, L., Sohmer, R., Gerwig,
1076 H., Wirtz, K., Meinhardt, F., Schwerin, A., Bath, O., Ma, N., and Wiedensohler, A.: Decreasing trends of particle
1077 number and black carbon mass concentrations at 16 observational sites in Germany from 2009 to 2018, *Atmos.*
1078 *Chem. Phys.*, 20(11), 7049–7068, <https://doi.org/10.5194/acp-20-7049-2020>, 2020.

1079 Sun, Y., Xu, W., Zhang, Q., Jiang, Q., Canonaco, F., Prévôt, A. S. H., Fu, P., Li, J., Jayne, J., Worsnop, D. R., and
1080 Wang, Z.: Source apportionment of organic aerosol from 2-year highly time-resolved measurements by an aerosol

1081 chemical speciation monitor in Beijing, China, *Atmos. Chem. Phys.*, 18(12), 8469–8489,
1082 <https://doi.org/10.5194/acp-18-8469-2018>, 2018.

1083 Tiitta, P., Leskinen, A., Hao, L., Yli-Pirilä, P., Kortelainen, M., Grigonyte, J., Tissari, J., Lamberg, H., Hartikainen, A.,
1084 Kuuspallo, K., Kortelainen, A. M., Virtanen, A., Lehtinen, K. E. J., Komppula, M., Pieber, S., Prévôt, A. S. H.,
1085 Onasch, T. B., Worsnop, D. R., Czech, H., Zimmermann, R., Jokiniemi, J., and Sippula, O.: Transformation of
1086 logwood combustion emissions in a smog chamber: Formation of secondary organic aerosol and changes in the
1087 primary organic aerosol upon daytime and night time aging, *Atmos. Chem. Phys.*, 16(20), 13251–13269,
1088 <https://doi.org/10.5194/acp-16-13251-2016>, 2016.

1089 Tobler, A., Skiba, A., Canonaco, F., Močnik, G., Rai, P., Chen, G., Bartyzel, J., Zimnoch, M., Styszko, K., Nęcki, J.,
1090 Furger, M., Róžański, K., Baltensperger, U., Slowik, J., and Prévôt, A.: Characterization of NR-PM1 and source
1091 apportionment of organic aerosol in Krakow, Poland, *Atmos. Chem. Phys.*, 1–22, <https://doi.org/10.5194/acp-2021-197>, 2021.

1093 Ulbrich, I. M., Canagaratna, M. R., Zhang, Q., Worsnop, D. R., and Jimenez, J. L.: Interpretation of organic components
1094 from Positive Matrix Factorization of aerosol mass spectrometric data, *Atmos. Chem. Phys.*, 9, [www.atmos-chem-](http://www.atmos-chem-phys.net/9/2891/2009/)
1095 [phys.net/9/2891/2009/](http://www.atmos-chem-phys.net/9/2891/2009/), 2009.

1096 van Pinxteren, D., Fomba, K. W., Spindler, G., Müller, K., Poulain, L., Iinuma, Y., Löschau, G., Hausmann, A., and
1097 Herrmann, H.: Regional air quality in Leipzig, Germany: Detailed source apportionment of size-resolved aerosol
1098 particles and comparison with the year 2000, *Faraday Discussions*, 189, 291–315,
1099 <https://doi.org/10.1039/c5fd00228a>, 2016.

1100 van Pinxteren, D., Mothes, F., Spindler, G., Fomba, K. W., Cuesta, A., Tuch, T., Müller, T., Wiedensohler, A., and
1101 Herrmann, H.: Zusatzbelastung aus Holzheizung, Sächsisches Landesamt für Umwelt, Landwirtschaft und
1102 Geologie (LfULG), Dresden, <https://publikationen.sachsen.de/bdb/artikel/36106>, 2020.

1103 Via, M., Minguillón, M. C., Reche, C., Querol, X., and Alastuey, A.: Increase of secondary organic aerosol over four
1104 years in an urban environment, *Atmos. Chem. Phys.*, 1–20, <https://doi.org/10.5194/acp-2020-1244>, 2020.

1105 Vlachou, A., Daellenbach, K., Bozzetti, C., Chazeau, B., Salazar, G., Szidat, S., Jaffrezo, J.-L., Hueglin, C.,
1106 Baltensperger, U., Haddad, I. el, Daellenbach, K. R., Salazar, G. A., and Prévôt, A. S. H.: Advanced source
1107 apportionment of carbonaceous aerosols by coupling offline AMS and radiocarbon size-segregated measurements
1108 over a nearly 2-year period, *Atmos. Chem. Phys.*, 18(9), 6187–6206, <https://doi.org/10.5194/acp-18-6187-2018>,
1109 2018.

1110 Vlachou, A., Tobler, A., Lamkaddam, H., Canonaco, F., Daellenbach, K. R., Jaffrezo, J. L., Minguillón, M. C.,
1111 Maasikmets, M., Teinmaa, E., Baltensperger, U., el Haddad, I., and Prévôt, A. S. H.: Development of a versatile
1112 source apportionment analysis based on positive matrix factorization: a case study of the seasonal variation of
1113 organic aerosol sources in Estonia, *Atmos. Chem. Phys.*, 19(11), 7279–7295, [https://doi.org/10.5194/acp-19-](https://doi.org/10.5194/acp-19-7279-2019)
1114 [7279-2019](https://doi.org/10.5194/acp-19-7279-2019), 2019.

1115 Wang, Y., Henning, S., Poulain, L., Lu, C., Stratmann, F., Wang, Y., Niu, S., Pöhlker, M., Herrmann, H., and
1116 Wiedensohler, A.: Aerosol activation characteristics and prediction at the central European ACTRIS research
1117 station of Melpitz, Germany, <https://doi.org/10.5194/acp-22-15943>, 2022.

1118 Wang, T., Fu, T., Chen, K., Cheng, R., Chen, S., Liu, J., Mei, M., Li, J., and Xue, Y.: Co-combustion behavior of dyeing
1119 sludge and rice husk by using TG-MS: Thermal conversion, gas evolution, and kinetic analyses, *Bioresource*
1120 *Technology*, 311, <https://doi.org/10.1016/j.biortech.2020.123527>, 2020.

1121 Watson, J. G.: Visibility: science and regulation, *J. Air Waste Manage.*, 52, 628-713,
1122 <https://doi.org/10.1080/10473289.2002.10470813>, 2002.

1123 Wehner, B., Philippin, S., and Wiedensohler, A.: Design and calibration of a thermodenuder with an improved heating
1124 unit to measure the size-dependent volatile fraction of aerosol particles, *Aerosol Science*, 33,
1125 www.elsevier.com/locate/jaerosci, 2002.

1126 WHO, Expert Consultation: [https://www.who.int/news-room/events/detail/2019/02/12/default-calendar/expert-](https://www.who.int/news-room/events/detail/2019/02/12/default-calendar/expert-consultation-risk-communication-and-intervention-to-reduce-exposure-and-to-minimize-the-health-effects-of-air-pollution)
1127 [consultation-risk-communication-and-intervention-to-reduce-exposure-and-to-minimize-the-health-effects-of-](https://www.who.int/news-room/events/detail/2019/02/12/default-calendar/expert-consultation-risk-communication-and-intervention-to-reduce-exposure-and-to-minimize-the-health-effects-of-air-pollution)
1128 [air-pollution](https://www.who.int/news-room/events/detail/2019/02/12/default-calendar/expert-consultation-risk-communication-and-intervention-to-reduce-exposure-and-to-minimize-the-health-effects-of-air-pollution), 2019.

1129 Wierońska-Wiśniewska, F., Makowska, D., and Strugała, A.: Arsenic in polish coals: Content, mode of occurrence, and
1130 distribution during coal combustion process, *Fuel*, 312, <https://doi.org/10.1016/j.fuel.2021.122992>, 2022.

1131 Xu, W., He, Y., Qiu, Y., Chen, C., Xie, C., Lei, L., Li, Z., Sun, J., Li, J., Fu, P., Wang, Z., Worsnop, D. R., and Sun, Y.:
1132 Mass spectral characterization of primary emissions and implications in source apportionment of organic aerosol,
1133 *Atmos. Meas. Tech.*, 13(6), 3205–3219, <https://doi.org/10.5194/amt-13-3205-2020>, 2020.

1134 Yang, S., Yuan, B., Peng, Y., Huang, S., Chen, W., Hu, W., Pei, C., Zhou, J., Parrish, D., Wang, W., He, X., Cheng, C.,
1135 Li, X., Yang, X., Song, Y., Wang, H., Qi, J., Wang, B., Wang, C., Wang, C., Wang, Z., Li, T., Zheng, E., Wang,
1136 S., Wu, C., Cai, M., Ye, C., Song, W., Cheng, P., Chen, D., Wang, X., Zhang, Z., Wang, X., Zheng, J., and Shao,
1137 M.: The formation and mitigation of nitrate pollution: comparison between urban and suburban environments,
1138 *ACP*, <https://doi.org/10.5194/acp-22-4539>, 2022.

1139 Yuan, J., Lewis Modini, R., Zanatta, M., Herber, A. B., Müller, T., Wehner, B., Poulain, L., Tuch, T., Baltensperger,
1140 U., and Gysel-Beer, M.: Variability in the mass absorption cross section of black carbon (BC) aerosols is driven
1141 by BC internal mixing state at a central European background site (Melpitz, Germany) in winter, *Atmos. Chem.*
1142 *Phys.*, 21(2), 635–655, <https://doi.org/10.5194/acp-21-635-2021>, 2021.

1143 Yudovich, Y. E., and Ketris, M. P.: Chlorine in coal: A review, In *International Journal of Coal Geology*, 67, Issues 1–
1144 2, pp. 127–144, <https://doi.org/10.1016/j.coal.2005.09.004>, 2006.

1145 Zhang, Q., Jimenez, J. L., Canagaratna, M. R., Ulbrich, I. M., Ng, N. L., Worsnop, D. R., and Sun, Y.: Understanding
1146 atmospheric organic aerosols via factor analysis of aerosol mass spectrometry: A review, In *Analytical and*
1147 *Bioanalytical Chemistry*, 401, Issue 10, pp. 3045–3067, <https://doi.org/10.1007/s00216-011-5355-y>, 2011.

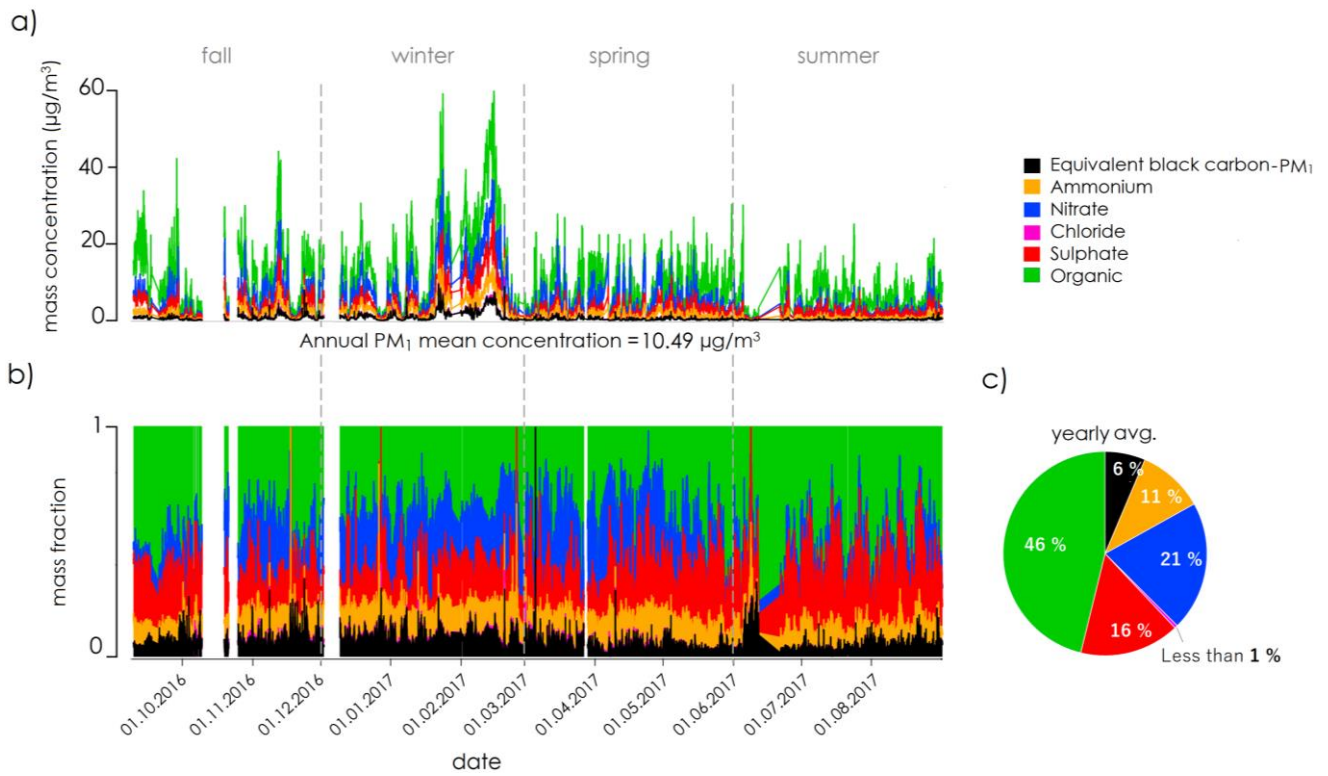
1148 Zhang, Q., Rami Alfarra, M., Worsnop, D. R., Allan, J. D., Coe, H., Canagaratna, M. R., and Jimenez, J. L.:
1149 Deconvolution and quantification of hydrocarbon-like and oxygenated organic aerosols based on aerosol mass
1150 spectrometry, *Environ. Sci. Technol.*, 39(13), 4938–4952, <https://doi.org/10.1021/es048568l>, 2005.

1151 Zhang, Y., Favez, O., Petit, J. E., Canonaco, F., Truong, F., Bonnaire, N., Crenn, V., Amodeo, T., Prévôt, A. S. H.,
1152 Sciare, J., Gros, V., and Albinet, A.: Six-year source apportionment of submicron organic aerosols from near-
1153 continuous highly time-resolved measurements at SIRTa (Paris area, France), *Atmos. Chem. Phys.*, 19(23),
1154 14755–14776, <https://doi.org/10.5194/acp-19-14755-2019>, 2019.

1155 Zhang, Y. J., Tang, L. L., Wang, Z., Yu, H. X., Sun, Y. L., Liu, D., Qin, W., Canonaco, F., Prévôt, A. S. H., Zhang, H.
1156 L., and Zhou, H. C.: Insights into characteristics, sources, and evolution of submicron aerosols during harvest
1157 seasons in the Yangtze River delta region, China, *Atmos. Chem. Phys.*, 15(3), 1331–1349,
1158 <https://doi.org/10.5194/acp-15-1331-2015>, 2015.

1159 Zhu, Q., Huang, X. F., Cao, L. M., Wei, L. T., Zhang, B., He, L. Y., Elser, M., Canonaco, F., Slowik, J. G., Bozzetti,
1160 C., El-Haddad, I., and Prévôt, A. S. H.: Improved source apportionment of organic aerosols in complex urban air
1161 pollution using the multilinear engine (ME-2), *Atmos. Meas. Tech.*, 11(2), 1049–1060,
1162 <https://doi.org/10.5194/amt-11-1049-2018>, 2018.

1163
1164
1165



1166

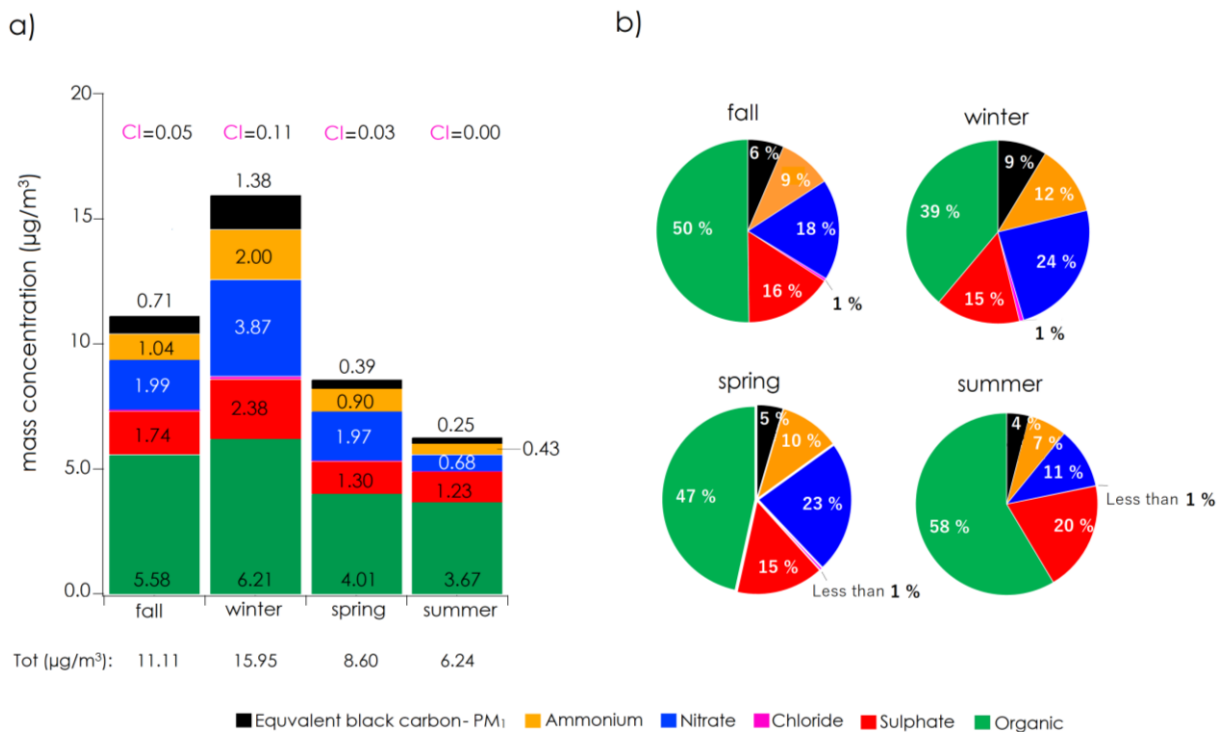
1167 **Fig. 1: Time series of a) the particulate PM₁ chemical composition, b) the corresponding mass fraction and c) average contribution**

1168

of each chemical component (time is in UTC).

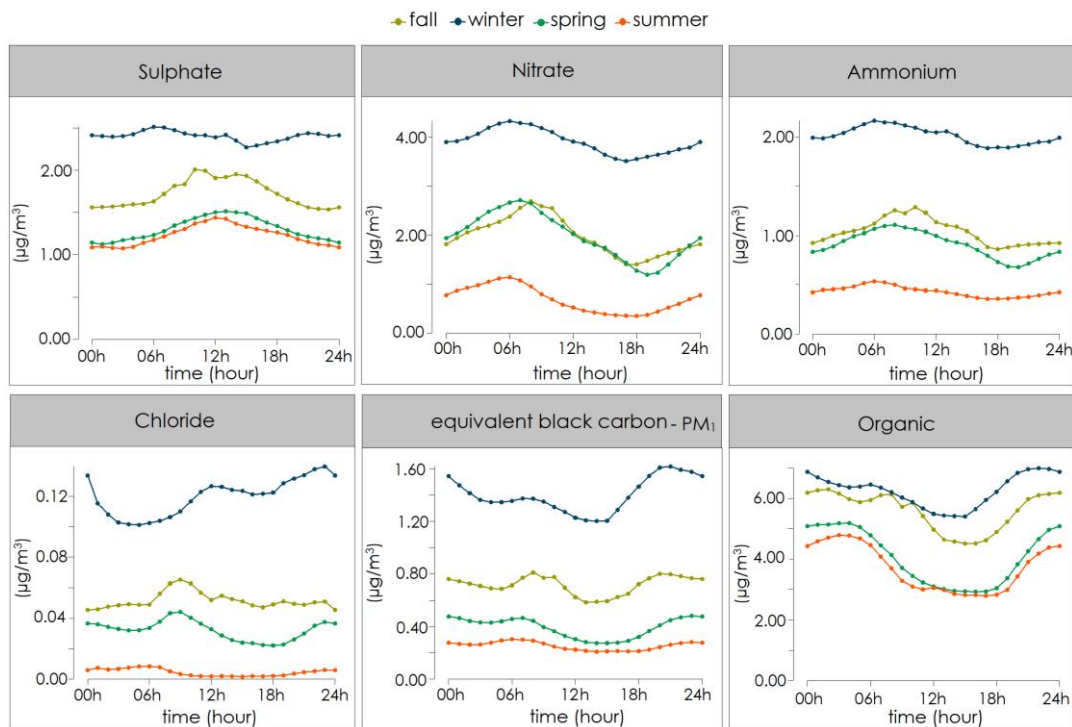
1169

1170



1171
1172

Fig. 2: seasonal variation of PM₁ a) absolute mass concentration and b) mass fraction.



1173
1174

Fig. 3: Seasonal diurnal cycle of PM₁ for ACSM organic and inorganic species (time is in UTC).

1175

1176

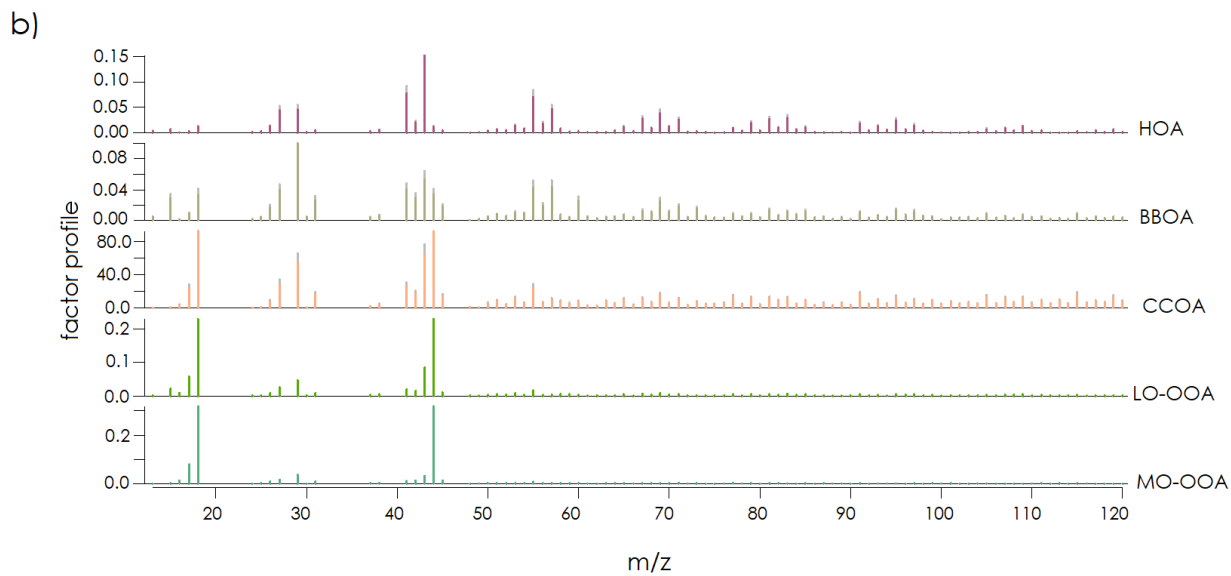
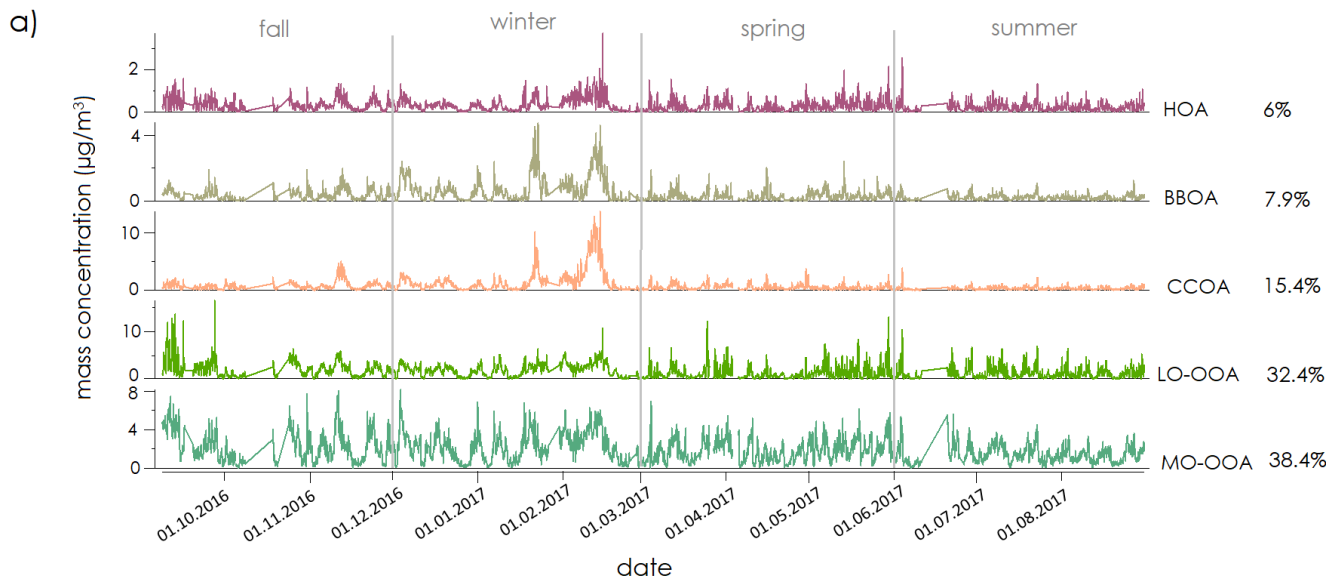
1177

Table 1: Seasonal/yearly mass concentration of each ACSM species, each PMF factors, contribution of the different POA-PMF-eBC-PM₁, and correlation of each factors with related species; PM₁.

| Species/ Factors | | Fall | Winter | Spring | Summer | Yearly |
|---|--|------|--------|--------|--------|--------|
| ACSM ($\mu\text{g}/\text{m}^3$) | Org | 5.58 | 6.21 | 4.01 | 3.67 | 4.84 |
| | SO ₄ ²⁻ | 1.74 | 2.38 | 1.30 | 1.23 | 1.67 |
| | NO ₃ ⁻ | 1.99 | 3.87 | 1.97 | 0.68 | 2.16 |
| | NH ₄ ⁺ | 1.04 | 2.00 | 0.90 | 0.43 | 1.11 |
| | Cl ⁻ | 0.05 | 0.11 | 0.03 | 0.00 | 0.05 |
| MAAP ($\mu\text{g}/\text{m}^3$) | eBC -PM ₁ | 0.71 | 1.38 | 0.39 | 0.25 | 0.66 |
| PMF ($\mu\text{g}/\text{m}^3$) | HOA | 0.35 | 0.36 | 0.27 | 0.23 | 0.30 |
| | BBOA | 0.36 | 0.72 | 0.27 | 0.21 | 0.39 |
| | CCOA | 0.72 | 1.58 | 0.47 | 0.30 | 0.77 |
| | LO-OOA | 2.13 | 1.95 | 1.24 | 1.26 | 1.62 |
| | MO-OOA | 2.21 | 2.25 | 1.82 | 1.44 | 1.92 |
| eBC-PM ₁ ($\mu\text{g}/\text{m}^3$) | eBC-PM ₁ -HOA | 0.16 | 0.19 | 0.03 | 0.04 | 0.05 |
| | eBC-PM ₁ -BBOA | 0.34 | 0.38 | 0.17 | 0.15 | 0.25 |
| | eBC-PM ₁ -CCOA | 0.23 | 0.74 | 0.16 | 0.02 | 0.37 |
| eBC-PM ₁ (%) | eBC-PM ₁ -HOA | 22 | 15 | 9 | 18 | 8 |
| | eBC-PM ₁ -BBOA | 47 | 29 | 47 | 69 | 37 |
| | eBC-PM ₁ -CCOA | 31 | 56 | 44 | 13 | 55 |
| Correlation (R ²) | HOA/ eBC-PM ₁ | 0.49 | 0.52 | 0.34 | 0.24 | 0.33 |
| | HOA/NO _x | 0.23 | 0.12 | 0.32 | 0.23 | 0.17 |
| | BBOA/Levo. | 0.19 | 0.59 | 0.09 | 0.07 | 0.54 |
| | BBOA/ eBC-PM ₁ | 0.62 | 0.81 | 0.48 | 0.42 | 0.77 |
| | CCOA/ eBC-PM ₁ | 0.65 | 0.85 | 0.49 | 0.30 | 0.82 |
| | CCOA/Cl ⁻ | 0.40 | 0.41 | 0.18 | 0.15 | 0.46 |
| | LO-OOA/ NO ₃ ⁻ | 0.22 | 0.59 | 0.01 | 0.12 | 0.19 |
| | LO-OOA/ SO ₄ ²⁻ | 0.36 | 0.55 | 0.00 | 0.02 | 0.23 |
| | MO-OOA / SO ₄ ²⁻ | 0.58 | 0.47 | 0.34 | 0.42 | 0.44 |
| | MO-OOA/ NO ₃ ⁻ | 0.24 | 0.47 | 0.16 | 0.24 | 0.31 |

1178

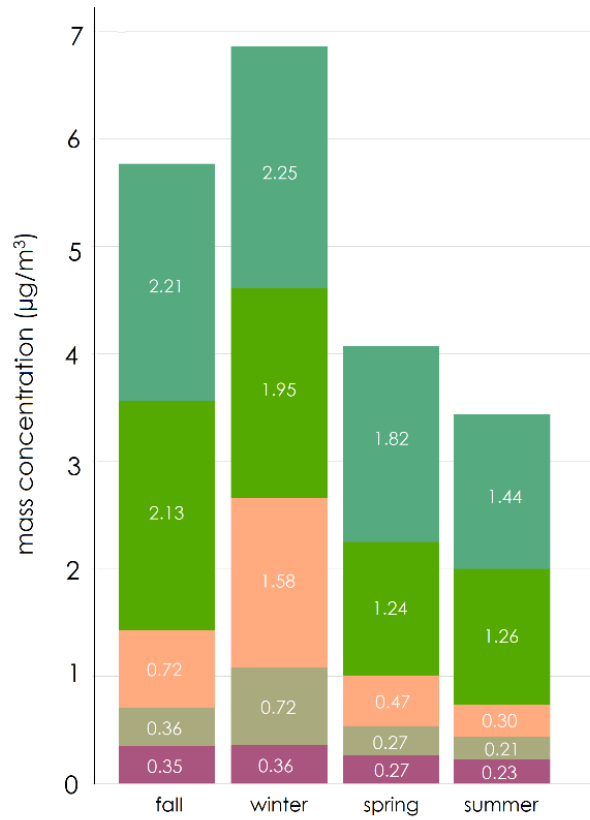
1179



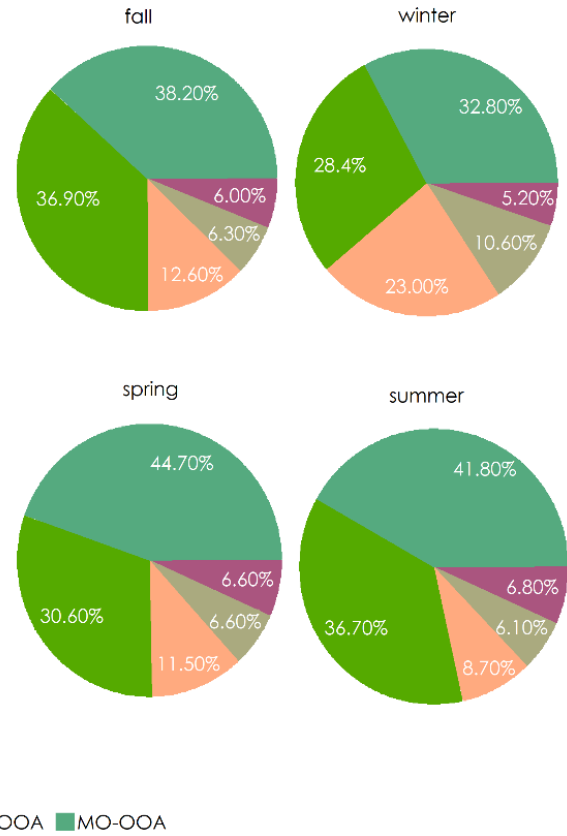
1180

1181 **Fig. 4: Overview of averaged PMF (ME-2) results, a) time series, and b) mass spectral profile of organic PMF factors (time is in**
 1182 **UTC).**

a)



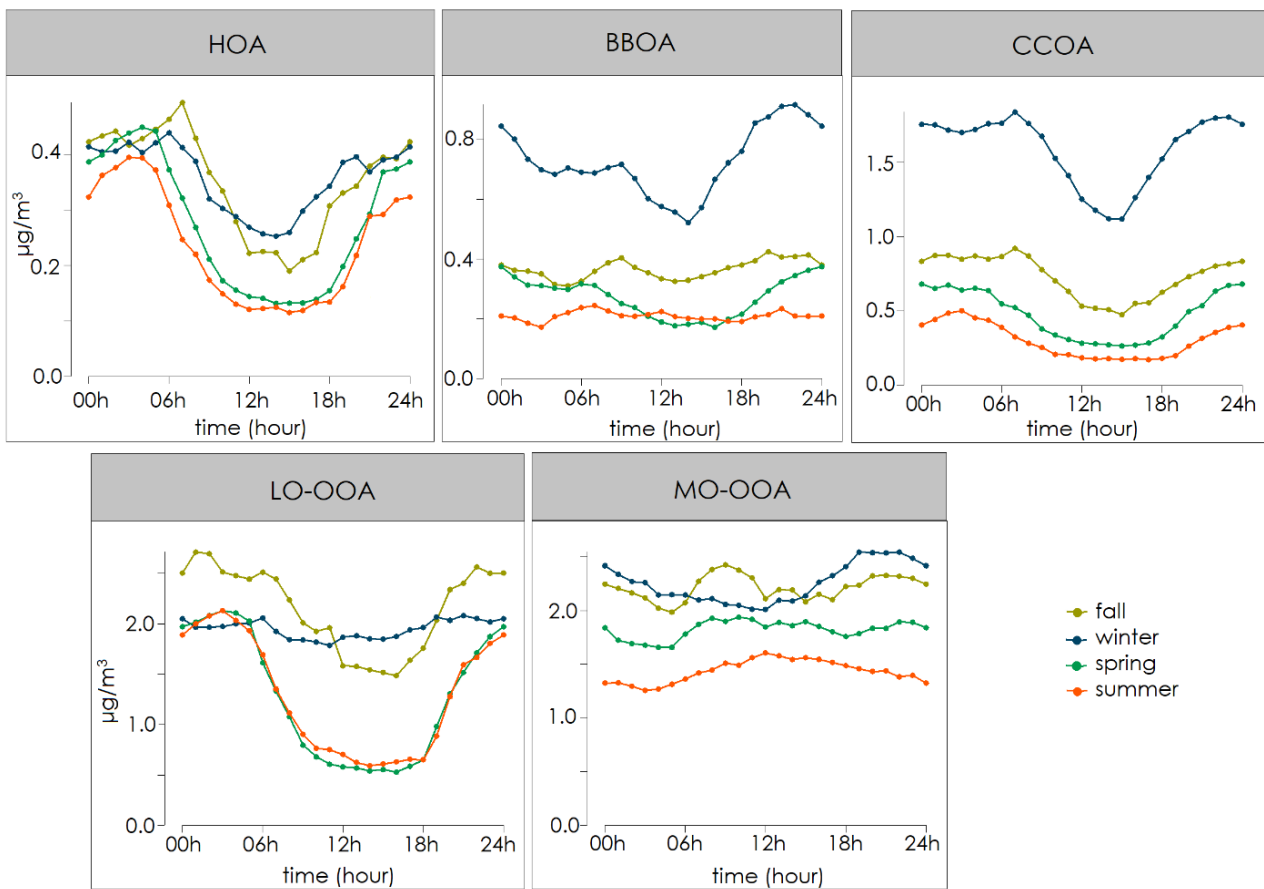
b)



1183

1184

Fig. 5: Seasonal variation of a) mass concentration, b) mass fraction of PMF source factors.



1185

1186 **Fig. 6: Seasonal diurnal cycle (hourly averages) of the organic components HOA, BBOA, CCOA, LO-OOA and MO-OOA in UTC**

1187

time.

1188

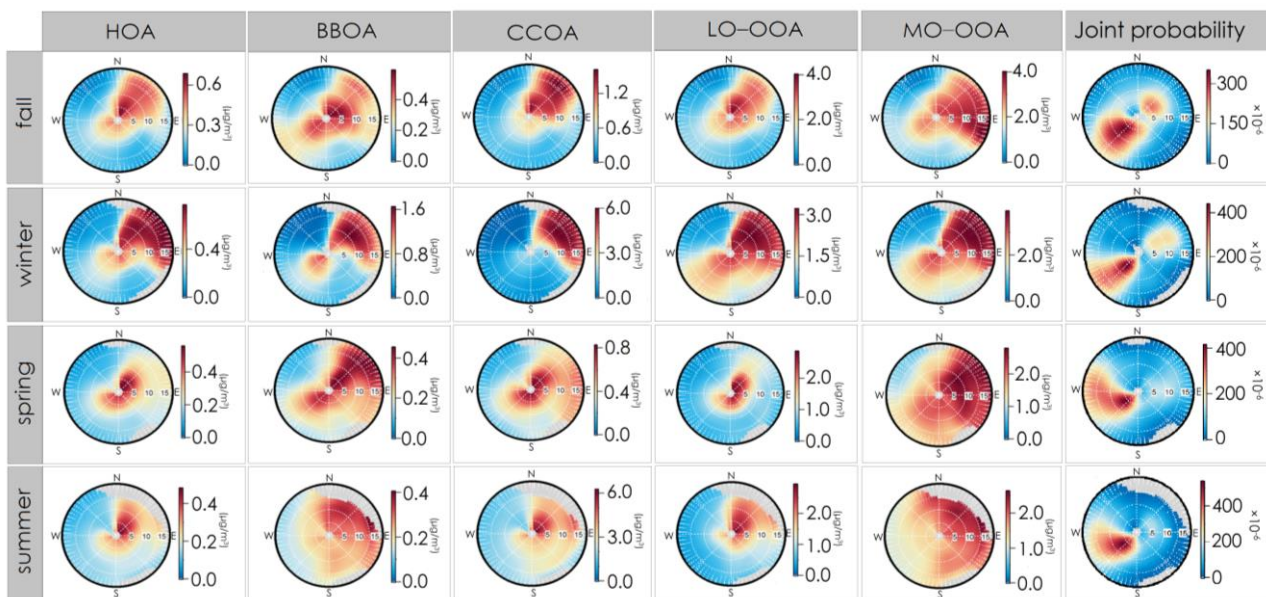
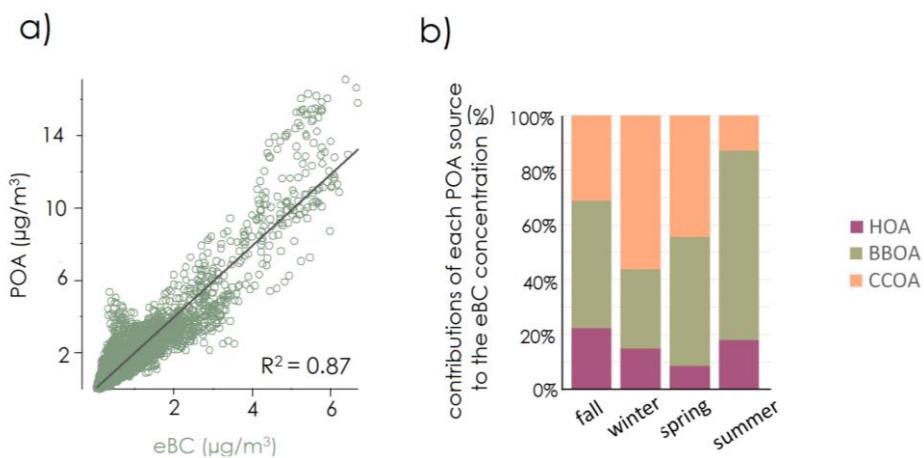


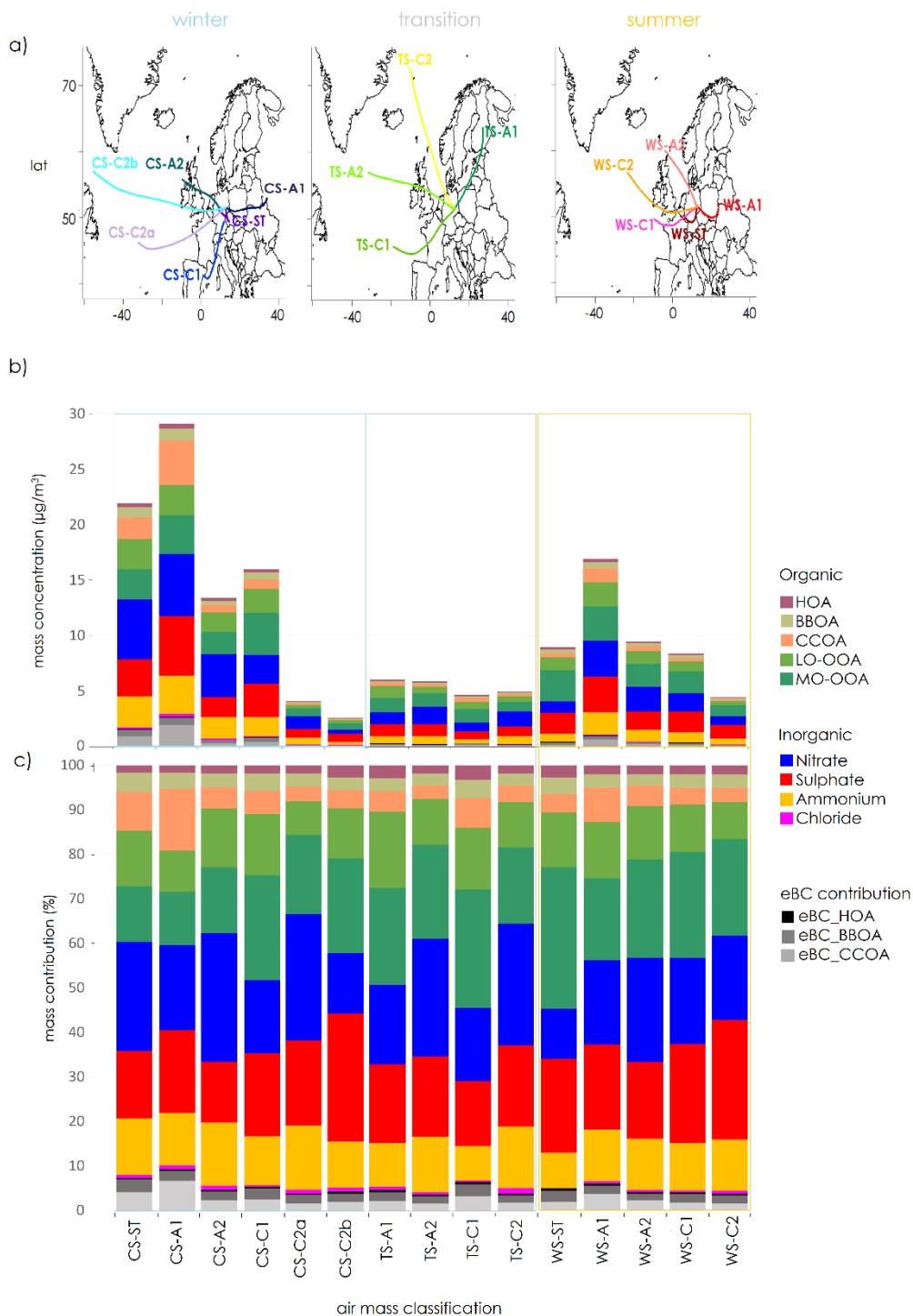
Fig. 7: Seasonal NWR plots for the different PMF factors (in $\mu\text{g}/\text{m}^3$).

1189
1190
1191



1192
1193
1194
1195
1196

Fig. 8: Contribution of the three POA factors to the mass concentration of eBC-PM_{10} , a) scatter plots POA vs eBC-PM_{10} and b) contributions of sources to the eBC-PM_{10} mass concentration.



1197

1198 **Fig. 9: a) air mass classification based on one-year backward trajectories cluster analysis at 12:00 UTC, b) influence of air mass to**

1199

the PM_{10} data and PMF factors, and c) contribution of them which averaged from 10:00 to 14:00 UTC.

1200

1201

1202

1203

1204

1205

Table. 2: Main statistical details of the 15 air mass types for total PM₁
 (CS=Cold Season, WS=Warm Season, ST=Stagnant, A=Anticyclonic, C=Cyclonic).

| Main season | Airmass type | Wind direction | Vorticity | Frequenc y (%) | Total mean (µg/m³) |
|--------------------------------------|---------------------|-----------------------|------------------|-------------------------------|--|
| Winter | CS-ST | Stagnating | Anticyclonic | 14 | 21.95 |
| | CS-A1 | East | Anticyclonic | 18 | 29.14 |
| | CS-A2 | West | Anticyclonic | 8 | 13.39 |
| | CS-C1 | South | Cyclonic | 10 | 15.99 |
| | CS-C2a | South West | Cyclonic | 3 | 04.09 |
| | CS-C2b | West | Cyclonic | 2 | 02.60 |
| Transition (Spring/ Fall) | TS-A1 | North East | Anticyclonic | 4 | 06.06 |
| | TS-A2 | West | Anticyclonic | 4 | 05.86 |
| | TS-C1 | South West | Cyclonic | 3 | 04.69 |
| | TS-C2 | North West | Cyclonic | 4 | 04.94 |
| Summer | WS-ST | Stagnating | Anticyclonic | 6 | 08.97 |
| | WS-A1 | South East | Anticyclonic | 11 | 16.95 |
| | WS-A2 | North West | Anticyclonic | 6 | 09.48 |
| | WS-C1 | West | Cyclonic | 5 | 08.41 |
| | WS-C2 | West | Cyclonic | 3 | 04.46 |

1206